Effective shadowing of transition maps for a Hamiltonian saddle-center-center equilibrium. Part II: numerical results*

Rodney L. Anderson†, Amadeu Delshams‡, Marian Gidea§, and Pablo Roldan¶

Abstract. This paper presents a semi-analytical and numerical methodology to compute, optimize, and shadow transition chains near normally hyperbolic invariant manifolds (NHIMs) in Hamiltonian systems, with a direct application to celestial mechanics and space mission design. We focus on the libration point L_1 of the Sun–Earth Spatial Restricted Three-Body Problem (SR3BP). To construct true trajectories from these pseudo-orbits, we introduce a specialized multiple shooting algorithm that combines analytical BNF motion near the NHIM with high-precision numerical integration far from the NHIM. Applying this algorithm to shadow a 16-iteration transition chain, we reduce the pseudo-trajectory position and velocity discontinuities ($\Delta x = 184,005$ km, $\Delta v = 338,000$ km/h) down to virtually zero error ($\Delta x < 1.5$ m, $\Delta v < 3 \times 10^{-5}$ m/s). The proposed method runs fully automatically and outperforms standard astrodynamics tools, such as two-level differential correction, by 1 to 2 orders of magnitude.

Key words. pseudotrajectories, shadowing, NHIM, Hamiltonian systems, homoclinic, heteroclinic orbits, invariant tori, normal forms, small divisors, transition map, scattering map, Arnol'd diffusion, Three-body problems, Spatial Restricted 3-Body Problem, Celestial mechanics

MSC codes. 37C50 (Primary) 37C29, 37J40, 70F07, 70F15 (Secondary)

1. Introduction.

Trajectories that visit designated regions of phase space in a prescribed sequence play a central role in celestial mechanics and modern space mission design. Near the collinear libration points (L_1 and L_2) of the Spatial Restricted Three-Body Problem (SR3BP), complex quasi-periodic orbits and their associated stable and unstable manifolds act as low-propulsion highways across interplanetary space. In particular, reaching high-inclination orbits relative to the ecliptic is of major scientific interest for heliophysics and out-of-ecliptic observation missions.

This paper addresses the computation, optimization, and high-precision numerical shadowing of transition chains, focusing on the Sun–Earth SR3BP at the libration point L_1. It is based on the classical geometric mechanism for global instability introduced by Arnold [2]. The mechanism relies on transition chains formed by transverse heteroclinic intersections between invariant tori on a Normally Hyperbolic Invariant Manifold (NHIM). In generic or non-perturbative settings with fixed parameters, long pseudo-orbits can be constructed by combining the *inner dynamics* (the restricted flow on the NHIM) with the *outer dynamics* along homoclinic channels.

The outer dynamics can be encoded either via the *scattering map* [5] or the *transition map* [6]. The scattering map relates the asymptotic past of a homoclinic point to its asymptotic future, while the transition map relates the projection onto the NHIM of the starting point of a homoclinic orbit segment to the projection onto the NHIM of the ending point of the segment. Although these two maps are conjugate under the flow, the transition map provides two key practical advantages: it is directly computable via standard numerical integration over finite-time homoclinic segments, and it explicitly preserves temporal information (transit times along homoclinic loops), which is crucial for evaluating total mission duration.

We obtain two transition maps $\{\tau_1, \tau_2\}$ associated to two different families of homoclinic

*Submitted to the editors Oct 26, 2026.

Funding: Part of the research presented in this paper has been carried out at the Jet Propulsion Laboratory, California Institute of Technology, under a contract with the National Aeronautics and Space Administration (80NM0018D0004). Research of M.G. was partially supported by NSF grant DMS-2154725 and DMS-2307718. Research of A.D and P.R. was partially supported by Spain's State Research Agency grant PID2024-158570NB-I00.

†Jet Propulsion Laboratory, California Institute of Technology.

‡Laboratory of Geometry and Dynamical Systems and IMTech, UPC.

§Department of Mathematical Sciences, Yeshiva University.

¶Departament de Matemàtiques, UPC. Corresponding author: Pablo.Roldan@upc.edu

segments. Then, we consider the Iterated Function System (IFS) $\{f, \tau_1, \tau_2\}$, formed by the inner map and the transition maps. We construct orbits of the IFS along which the vertical action I_{v} undergoes some significant gain. Then we develop an *efficient shadowing* strategy (in terms of travel time) that provides numerical trajectories that achieve the same gain (up to a small error). In particular, we consider a simple situation (motivated by our application to L_1 in the SR3BP) in which the IFS consists only of $\{\tau_1, \tau_2\}$, i.e., it consists of transition maps and not the inner map.

In the paper [8], a general theoretical foundation was established for Hamiltonian systems near a saddle-center-center equilibrium point. Constructive analytical and topological shadowing theorems were proved, establishing that finite guiding orbits of an Iterated Function System (IFS) of transition maps can be shadowed by true trajectories of the full system. While [8] constructively proved the existence of shadowing orbits, it provided no explicit numerical algorithm to locate them in realistic, non-perturbative applications.

We apply this methodology to the Spatial Restricted 3-Body Problem (SR3BP for short). This model describes the spatial dynamics of an infinitesimal body under the gravitational influence of two massive bodies that move on circular orbits about their center of mass. In this paper, the two massive bodies are the Sun and Earth, and the infinitesimal body represents a spacecraft. The motion of the spacecraft is described by a 3-degree-of-freedom Hamiltonian system. We consider the libration point L_1 located between the Sun and the Earth. A quasi-periodic orbit around L_1 has planar and vertical amplitude—relative to the ecliptic— I_{p} and I_{v}, which are action variables in Birkhoff normal form (BNF). We consider homoclinic orbits that go once around the Earth, and select two transition maps.

Following the methodology described for the general case [8], we construct true trajectories that exhibit a large variation in the vertical amplitude I_{v}. These vertical *drift trajectories* closely track a selected finite sequence of homoclinic segments associated with the transition maps. These are analogous to diffusion orbits in a perturbative setting, where the action variable changes by an amount of order one with respect to the parameter, i.e., independent of the perturbation size.

High-inclination orbits at the libration points are desirable for a variety of applications including studying the zodiacal dust cloud [23, 19] and they may also offer observations of the Sun's poles, not studied since the Ulysses mission [25]. Trajectories to these types of orbits have previously been studied using optimized low-thrust trajectories [24].

Another compelling possibility is the construction of long trajectories that visit designated regions of phase space in a prescribed order. This strategy has been widely proposed for space mission design [11, 15], where homoclinic and heteroclinic trajectories are combined to enable low-propulsion transfers between different invariant objects in the solar system [18, 4]. To our knowledge, this paper represents the first time that true trajectories shadowing transition chains of two or more homoclinic or heteroclinic orbits have been explicitly computed.

This paper are organized as follows. In Section 3 we recall the construction of Birkhoff normal form coordinates to obtain an integrable approximation of the flow in a neighborhood of the equilibrium point L_1, and we use it to describe local geometric structures, such as the NHIM and its associated unstable and stable invariant manifolds.

In Section 4 we review the transition and reduced transition maps.

In Section 5 we define several key concepts needed to construct drift trajectories for the original Hamiltonian system, such as *guiding orbits*, *pseudo-trajectories*, and *shadowing trajectories*.

In Section 6 we introduce a multiple shooting algorithm to find "numerical shadowing trajectories" that shadow a given guiding orbit of the IFS. The shadowing trajectory obtained is, in fact, the concatenation of several (high-precision) numerical integrations that match at the endpoints (up to a small numerical error).

In Section 7 we compute theoretical bounds for the size of the normal form and its reminder.

In Section 8 we compute the BNF of order $M = 16$ around the equilibrium point L_1. This allows us to explicitly compute the size of the normal form and its reminder and compare with the theoretical bounds. Moreover, we consider a neighborhood $U = U(\delta)$ of size $\delta = 0.1$ in the saddle BNF variables, and we show that the error in the orbit of BNF trajectories compared with the exact trajectories in $U(\delta)$ is less than 3×10^{-7}.

In Section 9 we obtain guiding orbits with the desired vertical action gain with a simple simulation of these two or more dynamics (inner and transition maps), leveraging the classic Dijkstra algorithm to find the shortest path in a graph. Then we apply our multiple shooting algorithm to shadow a guiding orbit within the Sun-Earth SR3BP consisting of 16 iterations of the transition map (corresponding to 16 homoclinic trajectories). The algorithm converges quickly thanks to a careful selection of the initial guess and produces a shadowing trajectory with a numerical error of 10^{-12}.

In Section 10 we use an alternative numerical method (two-level differential correction) to independently validate the shadowing trajectory obtained with multiple shooting. The differential corrector used here has been previously implemented in LTool [14, 16], which has been subsequently used for a range of missions including the Genesis mission [17, 26], the MoonRise Mission Concept [21], and some Europa Clipper studies [1].

The multiple shooting algorithm is able to reduce the total position and velocity error of the pseudo-trajectory from $\Delta x = 184\,005$ km and $\Delta v = 338\,000$ km/h, to virtually zero error in the shadowing trajectory ($\Delta x < 1.5$ m and $\Delta v < 0.00003$ m/s). This beats a state-of-the-art method like differential correction by 1-2 orders of magnitude. However, this is not surprising, given that the method of Section 6 has been developed for the special purpose of shadowing chains of homoclinic trajectories, while the method of Section 10 is more general purpose. An additional advantage is that the multiple shooting method runs automatically, while the differential corrector needs frequent intervention to heuristically select the number and location of patch points.

2. Main results.

We introduce a numerical method to find trajectories that shadow the guiding orbit. It is based on a multiple shooting scheme and an appropriate choice of initial guess. In fact, the method does not produce an exact shadowing trajectory, only a numerical approximation, but this is often enough for many practical applications. Moreover, this numerical approximation could theoretically be used as the seed for a computer assisted proof of a true shadowing orbit near it (see for example [13]).

Then, we study the Sun-Earth spatial R3BP around the Lagrange equilibrium point L_1. Using semi-analytical methods, we find the shortest-time drift guiding orbit in this particular setting, and then apply the multiple shooting scheme of Section 6 to shadow it.

Numerical Result 2.1. *Consider the SR3BP with a mass ratio given by* $\mu_{Sun\text{-}Earth} = 3.040423398444176 \cdot 10^{-6}$, *described in Section 7. Let the energy* H *be fixed to the value* $h = -1.50044$, *equivalent to a Jacobi constant* $C = -2H = 3.00088$.

(a) *Following [7], we obtain a semi-analytical approximation of the NHIM* Λ_h *around the equilibrium point* L_1 *using the BNF of order* $M = 16$.

(b) *Consider a neighborhood* $U = U(\delta)$ *of size* $\delta = 0.1$ *in the saddle BNF variables. In Section 8 we show that the error of the semi-analytical approximation of the NHIM in* $U(\delta)$ *is less than* 3×10^{-7}.

(c) *By part (b), the level sets of* I_{v} *are preserved by the inner map* f *up to an error of* $\varepsilon_1 = 3 \times 10^{-7}$. *In Section 9.1 we derive series representations for two different reduced transition maps* τ_1, τ_2 *that are globally defined on an annulus* $\mathcal{A} \subset \Lambda_h^{\Sigma}$, *corresponding to the range* $I_{\mathrm{v}} \in [I_1, I_2]$, *where* $I_1 = 0.001$ *and* $I_2 = 0.007$.

(d) *In Section 9.2 we find the orbit of the IFS* $\{f, \tau_1, \tau_2\}$ *that takes the least amount of time to drift from the lower boundary to the upper boundary in* $\mathcal{A}$. *See Figure 11a. It turns out that, in this particular scenario, the shortest-time drift orbit does not use the inner map* f; *it consists solely of iterates of the transition maps* τ_1, τ_2.

(e) *Let $(\boldsymbol{x}_i)_{i=1}^{17}$ be the guiding orbit of the IFS $\{\tau_1, \tau_2\}$ consisting of the last $N = 17$ points in the shortest-time drift orbit found in part (d). In Section 9.3, we apply the multiple shooting method of Section 6 to construct a (numerical) shadowing trajectory of the SR3BP close to the guiding orbit. The result is given in Table 2 and shown in Figure 13.*

It should be emphasized here that the trajectories found are true trajectories of the flow of SR3BP, that is, "zero cost" trajectories. If a slight increase in speed Delta v (Δv) (or a slight thrust) is allowed in the spacecraft, faster drift trajectories could be achieved, that is, trajectories that take less time. These would thus be "low cost" drift trajectories.

3. SR3BP and Birkhoff normal form. In this section, we introduce BNF coordinates to integrate the flow in a neighborhood of the equilibrium point L_1, and to describe the different invariant sets present in this neighborhood. For more details, see [8, Section 4].

The Hamiltonian of the SR3BP (Spatial Restricted 3 Body Problem) is

$$H = \frac{1}{2}\left(P_X^2 + P_Y^2 + P_Z^2\right) + YP_X - XP_Y - \frac{1-\mu}{r_1} - \frac{\mu}{r_2},$$

where $r_1^2 = r_{\mathrm{S}}^2 = (X-\mu)^2 + Y^2 + Z^2, r_2^2 = r_{\mathrm{E}}^2 = (X-\mu+1)^2 + Y^2 + Z^2$.

Following [7], we start by writing the Hamiltonian as a power series around the equilibrium point L_1. After translating the origin of coordinates to the equilibrium point, scaling to redefine the unit distance as the distance from L_1 to the Earth, introducing momenta p_x, p_y, p_z, and using Legendre polynomials to expand the nonlinear terms, we obtain the Hamiltonian (4.5) of [7], which has the form

$$H = \frac{1}{2}\left(p_x^2 + p_y^2 + p_z^2\right) + yp_x - xp_y - \sum_{n\geq 2} c_n(\mu)\varepsilon^n P_n\left(\frac{x}{\varepsilon}\right), \tag{3.1}$$

where the coefficients $c_n(\mu)$ are all of the same order of magnitude, $\varepsilon^2 = x^2 + y^2 + z^2$, and the effect of high-order terms is measured by the factor ε^n.

The linearized system has eigenvalues $\pm\lambda^0, \pm i\nu_{\mathrm{p}}^0, \pm i\nu_{\mathrm{v}}^0$, where $\lambda^0, \nu_{\mathrm{p}}^0, \nu_{\mathrm{v}}^0$ are real and positive (their values are given in section 7).

A symplectic linear change of variables

$$(x, y, z, p_x, p_y, p_z) = C(Q, P) = C(Q_1, Q_2, Q_3, P_1, P_2, P_3), \tag{3.2}$$

casts the quadratic part H_2 of H into its real normal form

$$H_2 = \lambda^0 Q_1 P_1 + \frac{\nu_{\mathrm{p}}^0}{2}\left(Q_2^2 + P_2^2\right) + \frac{\nu_{\mathrm{v}}^0}{2}\left(Q_3^2 + P_3^2\right).$$

We can construct the BNF of order $M \geq 2$ provided that the so called *small divisors* associated with the equilibrium point L_1 remain strictly positive for all $s = 2, \ldots, M$. These small divisors are defined as follows:

$$\alpha_s = \alpha_s(\mu) = \min\left|k_{\mathrm{s}}\lambda^0 + i\left(k_{\mathrm{p}}\nu_{\mathrm{p}}^0 + k_{\mathrm{v}}\nu_{\mathrm{v}}^0\right)\right| = \min\sqrt{k_{\mathrm{s}}^2\left(\lambda^0\right)^2 + \left(k_{\mathrm{p}}\nu_{\mathrm{p}}^0 + k_{\mathrm{v}}\nu_{\mathrm{v}}^0\right)^2} > 0, \tag{3.3}$$

where the minimum is taken over all $k_{\mathrm{s}}, k_{\mathrm{p}}, k_{\mathrm{v}} \in \mathbb{Z}$ so that $0 < |k_{\mathrm{s}}| + |k_{\mathrm{p}}| + |k_{\mathrm{v}}| \leq s$.

Then, there exist a neighborhood $U^{(M)}$ of the origin and a near-identity symplectic transformation $\Psi^{(M)}\colon\ U^{(M)} \mapsto \mathbb{R}^6$, $(Q, P) = \Psi^{(M)}(q, p)$, which puts the system in normal form up to order M, namely,

$$\mathcal{H}^{(M)} := H \circ \Psi^{(M)} = H_2 + \mathcal{Z}^{(M)}(I) + \mathcal{R}^{(M)}(q, p).$$

The truncated Hamiltonian $H_2 + \mathcal{Z}^{(M)}$ depends only on the *action variables* $\boldsymbol{I} = (I_{\mathrm{s}}, I_{\mathrm{p}}, I_{\mathrm{v}})$, where $I_{\mathrm{s}} = xy$, with $x = q_1$, $y = p_1$, $I_{\mathrm{p}} = \dfrac{q_2^2 + p_2^2}{2}$, $I_{\mathrm{v}} = \dfrac{q_3^2 + p_3^2}{2}$.

Let $\phi = (\phi_{\mathrm{p}}, \phi_{\mathrm{v}})$ be the *angle variables* symplectic conjugate to the actions $I = (I_{\mathrm{p}}, I_{\mathrm{v}})$.

Remark 3.1. The reminder $\mathcal{R}^{(M)}$ is very small in a sufficiently small neighborhood of the origin. We give precise bounds in Sections 7 and 8.

The new coordinates (x, y, I, ϕ) will be called *Birkhoff normal form coordinates*. They are defined in a neighborhood

$$U = U(\delta, r) = \left\{ \boldsymbol{K} = (x, y, I, \phi) \in [-\delta, \delta]^2 \times [0, r]^2 \times \mathbb{T}^2 \right\}. \tag{3.4}$$

The variables (x, y) correspond to the hyperbolic component of the dynamics. The NHIM near L_1 corresponds to $I_{\mathrm{s}} = xy = 0$. The action-angle pair $(I_{\mathrm{p}}, \phi_{\mathrm{p}})$ corresponds to the 'planar component', whereas $(I_{\mathrm{v}}, \phi_{\mathrm{v}})$ corresponds to the 'vertical component'.

If we neglect the remainder $\mathcal{R}$, the flow inside U is simply given by the normal form $H_2 + \mathcal{Z}(\boldsymbol{I})$. Abusing notation, we will also denote the BNF flow by Φ_t. It takes the explicit form

$$x(t) = \mathrm{e}^{t\lambda} x(0), \quad y(t) = \mathrm{e}^{-t\lambda} y(0), \qquad I(t) = I(0), \quad \phi(t) = \phi(0) + t\nu, \tag{3.5}$$

where we have introduced the notation

$$\lambda \coloneqq \frac{\partial \mathcal{Z}}{\partial I_{\mathrm{s}}} = \frac{\partial \mathcal{Z}}{\partial I_{\mathrm{s}}}(\boldsymbol{I}) = \lambda^0 + O(\boldsymbol{I}) = \frac{\partial \mathcal{Z}}{\partial I_{\mathrm{s}}}(\boldsymbol{I}(0)), \tag{3.6}$$

$$\nu \coloneqq \frac{\partial \mathcal{Z}}{\partial I} = \nabla_I \mathcal{Z}(\boldsymbol{I}) = \nu^0 + O(\boldsymbol{I}) = \nabla_I \mathcal{Z}(\boldsymbol{I}(0)). \tag{3.7}$$

Thanks to the explicit expression (3.5) for the trajectories in U, the description of the most important invariants sets within U, such as the NHIM, and their associated stable/unstable manifolds, is straigthforward using normal form coordinates.

First, let us denote

$$\Lambda = W^{\mathrm{c}}_{\mathrm{loc}} = \{\boldsymbol{X} = (x = 0, y = 0, I, \phi\} = \{(0, 0, I, \phi)\} = \{(0, 0)\} \times [0, r]^2 \times \mathbb{T}^2$$

the local center manifold of L provided by the normal form, which is a 4-dimensional NHIM.

Any point $\boldsymbol{X} = (0, 0, I, \phi) \in \Lambda$ has associated *local stable and unstable fibers* in U

$$W^{\mathrm{s}}_{\mathrm{loc}}(\boldsymbol{X}) = \{\boldsymbol{Z} = (x = 0, y, I, \phi),\ |y| \le \delta\},\ W^{\mathrm{u}}_{\mathrm{loc}}(\boldsymbol{X}) = \{\boldsymbol{Z} = (x, y = 0, I, \phi),\ |x| \le \delta\},$$

which can be extended outside U by the backward and forward flow, respectively, to form the global stable and unstable fibers $W^{\mathrm{s}}(\boldsymbol{X})$ and $W^{\mathrm{u}}(\boldsymbol{X})$. Their unions on $\boldsymbol{X} \in \Lambda$ form the stable and unstable *invariant* manifolds of the NHIM Λ

$$W^{\mathrm{s}}(\Lambda) = \bigcup_{\boldsymbol{X} \in \Lambda} W^{\mathrm{s}}(\boldsymbol{X}), \qquad W^{\mathrm{u}}(\Lambda) = \bigcup_{\boldsymbol{X} \in \Lambda} W^{\mathrm{u}}(\boldsymbol{X}).$$

4. Transition map in BNF coordinates.

In this section, we introduce the transition and reduced transition maps. For more details, see [8, Section 5].

Let U be the BNF domain given by Equation (3.4). We think of int U as the *interior* domain, containing the NHIM Λ, and out U as the *exterior* domain, containing the homoclinic channel Γ.

Definition 4.1 (Sections). *We define the following local Poincaré sections for the flow. The* incoming boundary *is given by* $\Sigma_+ \coloneqq \{\boldsymbol{K} = (x, y, I, \phi) \in \partial U : y = \pm\delta\}$, *while the* outgoing boundary *is given by* $\Sigma_- \coloneqq \{\boldsymbol{K} = (x, y, I, \phi) \in \partial U : x = \pm\delta\}$. *We also define the section* $\Sigma = \{\boldsymbol{K} = (x, y, I, \phi) \in \partial U : \phi_p = 0\}$.

4.1. Transition map.

We recall how the homoclinic orbits are computed following [7]. Let $\boldsymbol{Z}_- \in W^u(\Lambda)$ and $\boldsymbol{Z}_+ \in W^s(\Lambda)$ be two arbitrary points in the outgoing (resp. incoming) boundary section of the BNF domain U, with coordinates

$$\boldsymbol{Z}_- = (\delta, 0, I_-, \phi_-) \in \Sigma_- \subset \partial U$$
$$\boldsymbol{Z}_+ = (0, \delta, I_+, \phi_+) \in \Sigma_+ \subset \partial U.$$

(For simplicity, we consider the case $x = y = \delta > 0$, but x or $y = -\delta < 0$ is analogous). The variables (I_-, ϕ_-) and (I_+, ϕ_+) determine $\boldsymbol{Z}_-$ and $\boldsymbol{Z}_+$, and they are parameters to be found during the procedure.

Numerically integrate the trajectory starting at $\boldsymbol{Z}_-$ forward in time until it intersects some exterior section $\mathscr{S}$ at a point $\mathcal{K}_- = \Phi_{T_-}(\boldsymbol{Z}_-)$. Similarly, integrate the trajectory starting at $\boldsymbol{Z}_+$ backward in time until it intersects $\mathscr{S}$ at a point $\mathcal{K}_+ = \Phi_{T_+}(\boldsymbol{Z}_+)$. To find a homoclinic, iteratively correct (I_-, ϕ_-) and (I_+, ϕ_+) using a Newton-like method, until $\mathcal{K}_+ = \mathcal{K}_- = \mathcal{K}$.

Notice that $[\boldsymbol{Z}_-, \boldsymbol{Z}_+]$ is a finite time homoclinic orbit segment of length $T_{\text{ext}} = T_- + T_+$.

Remark 4.2. These type of homoclinic intersections at the "first cut" of the asymptotic manifolds with $\mathscr{S}$ are usually called *primary* or *one-round homoclinics*.

Assume that $\mathcal{K}$ belongs to a homoclinic channel Γ as defined in [8, Section 2]. Using BNF coordinates, we can project the points $\boldsymbol{Z}_\pm$ onto the NHIM. Indeed, $\boldsymbol{Z}_+ \in W^{\mathrm{s}}(\boldsymbol{X}_+)$, where $\boldsymbol{X}_+ = (0, 0, I_+, \phi_+) \in \Lambda$. Analogously, $\boldsymbol{Z}_- \in W^{\mathrm{u}}(\boldsymbol{X}_-)$ where $\boldsymbol{X}_- = (0, 0, I_-, \phi_-) \in \Lambda$.

As shown in [8], the transition map $\mathcal{T}\colon \Lambda \to \Lambda$, is simply the map that associates X_- with X_+, given in BNF coordinates by

$$\boldsymbol{X}_- = (I_-, \phi_-) \mapsto \boldsymbol{X}_+ = (I_+, \phi_+).$$

4.2. Reduced transition map. It is convenient to reduce the dimension of the phase space and invariant objects, as well as the transition map $\mathcal{T}$. We do so by fixing the energy value and passing from the flow to a Poincaré map.

The original Hamiltonian system has a conserved quantity, the energy H, or, equivalently, the Jacobi constant $C = -2H$. For a fixed energy $H = h > h^0$ or a fixed Jacobi constant $C = c < c_0$ the action I_{p} can be given as an implicit function of $I_{\mathrm{s}}, I_{\mathrm{v}}, h$: $I_{\mathrm{p}} = f_h(I_{\mathrm{s}}, I_{\mathrm{v}})$. The corresponding 3-dimensional NHIM on the level of energy $H = h$ is given by $\Lambda_h = \Lambda \cap \{H = h\}$ and is parameterized by the variables $\phi_{\mathrm{p}}, \phi_{\mathrm{v}}, I_{\mathrm{v}}$.

Then consider the Poincaré section Σ within U, with associated Poincaré map $\mathcal{F}$. We denote

$$\Lambda_h^\Sigma = \Lambda_h \cap \Sigma = \{\boldsymbol{x} = (0, 0, I, \phi) : \phi_{\mathrm{p}} = 0, I_{\mathrm{p}} = f_h(0, I_{\mathrm{v}}), I_{\mathrm{v}} \in [0, r], \phi_{\mathrm{v}} \in \mathbb{T}\}$$

the 2-dimensional NHIM of $\mathcal{F}$, which is parameterized by the variables $\phi_{\mathrm{v}}, I_{\mathrm{v}}$.

Next, we compute the 2-dimensional reduced transition map $\tau\colon \Lambda_h^\Sigma \to \Lambda_h^\Sigma$ associated to $\mathcal{F}$. The construction is analogous to the (3-dimensional) transition map, but we start 'shooting' from the section Σ instead of $\Sigma_\pm$.

Let $\boldsymbol{T}_\pm \geq T_\pm$ be the first times such that the forward and backward trajectories of $\mathcal{K} \in \Gamma$ reach the section $\Sigma = \{\phi_{\mathrm{p}} = 0\}$ inside U, at the new points $\boldsymbol{z}_\pm \in \Sigma$.

Using BNF coordinates, we can project the points $\boldsymbol{z}_\pm$ onto the NHIM Λ_h^Σ. Indeed, $\boldsymbol{z}_+ \in W^{\mathrm{s}}(\boldsymbol{x}_+)$ and $\boldsymbol{z}_- \in W^{\mathrm{u}}(\boldsymbol{x}_-)$, where

$$\begin{aligned} \boldsymbol{x}_+ &= \big(0, 0, I_+, \widetilde{\phi}_+\big) \in \Lambda_h^\Sigma, \\ \boldsymbol{x}_- &= \big(0, 0, I_-, \widetilde{\phi}_-\big) \in \Lambda_h^\Sigma. \end{aligned}$$

The reduced transition map $\tau\colon \Lambda_h^\Sigma \to \Lambda_h^\Sigma$, is the map that associates $\boldsymbol{x}_-$ with $\boldsymbol{x}_+$, given in BNF coordinates by

$$\boldsymbol{x}_- = (I_{-,\mathrm{v}}, \widetilde{\phi}_{-,\mathrm{v}}) \mapsto \boldsymbol{x}_+ = (I_{+,\mathrm{v}}, \widetilde{\phi}_{+,\mathrm{v}}).$$

5. Pseudo-trajectories and shadowing trajectories. This section defines in a precise way several key concepts that we will later need to construct drift trajectories for the original Hamiltonian system Φ_t. In particular, we introduce

- a *guiding orbit* as an orbit of an IFS consisting of the inner dynamics and (reduced) transition maps;
- a *pseudo-trajectory* as a sequence of trajectory segments of the flow Φ_t that form an almost continuous trajectory, and

- a *shadowing trajectory* as a true trajectory of the flow Φ_t that is "close" to a pseudo-trajectory.

The reader is referred to Section 9 for an illustration of these concepts in the SR3BP system. In particular, see an example of guiding orbits in Figure 11, a pseudo-trajectory in Figure 12, and the corresponding shadowing trajectory in Figure 13.

Definition 5.1. *Let $\tau_1, \tau_2, \dots, \tau_L$ be reduced transition maps defined on Λ_h^Σ. Any finite orbit of the IFS $\{f, \tau_1, \dots, \tau_L\}$ consisting of the inner map and transition maps will be referred to as a* guiding orbit.

In particular, we will consider guiding orbits of a special type, generated solely by transition maps, i.e., $(\boldsymbol{x}_i)_{i=1}^N$ in Λ_h^Σ such that $\tau_{\alpha(i)}(\boldsymbol{x}_i) = \boldsymbol{x}_{i+1}$, where $\alpha(i) \in \{1, 2, \dots, L\}$. These guiding orbits are important since they minimize the drift time (when $\delta = 0.1$); see Section 9.2. Therefore, the main Numerical Result 2.1 is concerned with shadowing of guiding orbits of this type.

Recall that transition maps encode the homoclinic dynamics to Λ_h^Σ, so the points $\boldsymbol{x}_i$ in a guiding orbit do not belong to a true trajectory of the original system. To each guiding orbit, we associate a *sequence of Λ_h-homoclinic trajectories* such that each homoclinic synchronizes with the next homoclinic in the sequence in the following way. As explained in Section 4, for any homoclinic point $\mathcal{K} \in W^{\mathrm{u}}(\Lambda) \cap W^{\mathrm{s}}(\Lambda)$, there exist

- unique times $T_\pm > 0$ such that $\boldsymbol{Z}_\pm = \Phi_{\pm T_\pm}(\mathcal{K}) \in \Sigma_\pm \subset \partial U$, and
- unique times $\boldsymbol{T}_\pm = T_\pm + t_\pm$ with $t_\pm > 0$, such that $\boldsymbol{z}_\pm = \Phi_{\pm \boldsymbol{T}_\pm}(\mathcal{K}) \in U_h^\Sigma$ has zero planar angle: $\phi_{\mathrm{p},\pm} = 0$ in $\boldsymbol{z}_\pm$.

Remark 5.2. $\boldsymbol{Z}_\pm$ and $\boldsymbol{z}_\pm$ are simply related by the flow: $\boldsymbol{z}_\pm = \Phi_{\pm t_\pm}(\boldsymbol{Z}_\pm)$.

Let the guiding orbit be fixed. To each iterate

$$\boldsymbol{x}_i = (0, 0, I^i, \phi^i) \in \Lambda_h^\Sigma, \text{ with } I^i_{\mathrm{p}} = f_h(0, I^i_{\mathrm{v}}), \phi^i_{\mathrm{p}} = 0, \tag{5.1}$$

in the guiding orbit, associate the points

$$\begin{aligned} \boldsymbol{z}_i^+ &= \left(0, y = \rho_+^i := \exp\left(-t_+^i\, \lambda\right) \delta, I^i, \phi^i\right) \in W^{\mathrm{s}}(\boldsymbol{x}_i) \subset W^{\mathrm{s}}(\Lambda_h^\Sigma), \\ \boldsymbol{z}_i^- &= \left(x = \rho_-^i := \exp\left(-t_-^i\, \lambda\right) \delta, 0, I^i, \phi^i\right) \in W^{\mathrm{u}}(\boldsymbol{x}_i) \subset W^{\mathrm{u}}(\Lambda_h^\Sigma), \end{aligned} \tag{5.2}$$

and

$$\begin{aligned} \boldsymbol{Z}_i^+ &= \Phi_{-t_+^i}(\boldsymbol{z}_i^+) = \left(0, y = \delta, I^i, \phi_+^i = \phi^i - t_+^i\, \nu\right) \in W^{\mathrm{s}}(\Phi_{-t_+^i}(\boldsymbol{x}_i)) \cap \Sigma_+, \\ \boldsymbol{Z}_i^- &= \Phi_{t_-^i}(\boldsymbol{z}_i^-) = \left(x = \delta, 0, I^i, \phi_-^i = \phi^i + t_-^i\, \nu\right) \in W^{\mathrm{u}}(\Phi_{t_-^i}(\boldsymbol{x}_i)) \cap \Sigma_-, \end{aligned} \tag{5.3}$$

where λ, ν, defined in equations (3.6–3.7), are evaluated on $\boldsymbol{I} = (0, I^i) = (0, I^i_{\mathrm{p}}, I^i_{\mathrm{v}})$.

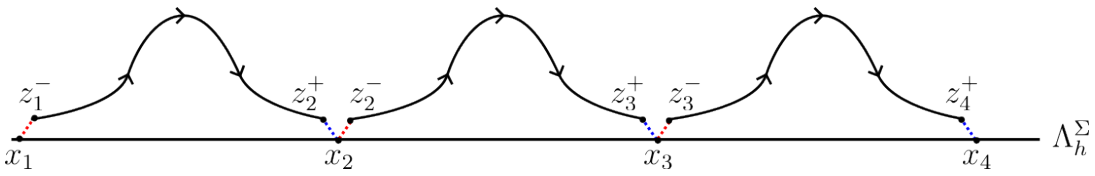


Figure 1: Schematic figure showing a guiding orbit $(\boldsymbol{x}_i)_{i=1}^4 \in \Lambda_h^\Sigma$ and the corresponding reduced pseudo-trajectory $(\boldsymbol{z}_i^-, \boldsymbol{z}_{i+1}^+)_{i=1}^3$. Finite homoclinic trajectory segments corresponding to the reduced pseudo-trajectory are shown in black; unstable fibers in red, stable fibers in blue. See also Figure 12 for a numerical example.

Definition 5.3. *The sequence of pairs $(\boldsymbol{Z}_i^-, \boldsymbol{Z}_{i+1}^+)_{i=1}^{N-1}$ will be called a* pseudo-trajectory *of the system, while the sequence of pairs $(\boldsymbol{z}_i^-, \boldsymbol{z}_{i+1}^+)_{i=1}^{N-1}$ will be called a* reduced pseudo-trajectory.

They satisfy the following conditions:

1. For every $i = 1, \dots, N-1$, the pair $(\boldsymbol{Z}_i^-, \boldsymbol{Z}_{i+1}^+)$ are the endpoints in ∂U of a (finite-time $T_{\text{ext}}^i = T_-^i + T_+^{i+1}$) homoclinic trajectory, i.e. there exists a homoclinic point $\mathcal{K}_i \in W^{\text{u}}(\Lambda) \cap W^{\text{s}}(\Lambda)$ and times T_-^i, T_+^{i+1} such that

$$\boldsymbol{Z}_i^- = \Phi_{-T_-^i}(\mathcal{K}_i) \qquad \text{and} \qquad \boldsymbol{Z}_{i+1}^+ = \Phi_{T_+^{i+1}}(\mathcal{K}_i).$$

2. For every $i = 2, 3, \dots, N-1$, the forward trajectory of $\boldsymbol{z}_i^+$ and the backward trajectory of $\boldsymbol{z}_i^-$ synchronize to the same orbit: As $t \to \infty$, we have

$$\left\|\Phi_t(\boldsymbol{z}_i^+) - \Phi_t(\boldsymbol{x}_i)\right\| \to 0 \qquad \text{and} \qquad \left\|\Phi_{-t}(\boldsymbol{z}_i^-) - \Phi_{-t}(\boldsymbol{x}_i)\right\| \to 0.$$

By Remark 5.2, the forward trajectory of $\boldsymbol{Z}_i^+$ and the backward trajectory of $\boldsymbol{Z}_i^-$ also tend to the same orbit: As $t \to \infty$, we have

$$\left\|\Phi_{t+t_+}(\boldsymbol{Z}_i^+) - \Phi_t(\boldsymbol{x}_i)\right\| \to 0 \qquad \text{and} \qquad \left\|\Phi_{-(t+t_-)}(\boldsymbol{Z}_i^-) - \Phi_{-t}(\boldsymbol{x}_i)\right\| \to 0.$$

Remark 5.4. The sequence of points $(\boldsymbol{z}_i^-)_{i=1}^{N-1}$ determines a finite *pseudo-orbit* in the classical sense of dynamical systems [3, 13]: there is an associated sequence $(h_i)_{i=1}^{N-2}$ of positive times, $h_i = T_{\text{ext}}^i + t_-^i + t_+^{i+1}$, such that

$$\left\|\boldsymbol{z}_{i+1}^- - \Phi^{h_i}(\boldsymbol{z}_i^-)\right\| \le \delta \quad \text{for } i = 1, \dots, N-2,$$

where we are using the maximum norm. Notice that $\Phi^{h_i}(\boldsymbol{z}_i^-) = \boldsymbol{z}_{i+1}^+$. Indeed, for all i, both points $\boldsymbol{z}_i^-$ and $\boldsymbol{z}_i^+$ are δ-close to $\boldsymbol{x}_i$:

$$\left\|\boldsymbol{z}_i^+ - \boldsymbol{x}_i\right\| = |y| = \rho_+ := \mathrm{e}^{-t_+\lambda}\delta \le \delta,$$
$$\left\|\boldsymbol{z}_i^+ - \boldsymbol{x}_i\right\| = |x| = \rho_- := \mathrm{e}^{-t_-\lambda}\delta \le \delta.$$

In our particular scenario, pseudo-orbits specifically consist of points on homoclinic orbits to Λ_h^Σ, not general orbits. See Figure 1.

Definition 5.5. *A* shadowing trajectory *is a trajectory of the system that passes close to the pseudo-trajectory, i.e., close to all the points* $(\boldsymbol{Z}_i^-, \boldsymbol{Z}_{i+1}^+)_{i=1}^{N-1}$.

Given a pseudo-trajectory, our goal is to find a trajectory that shadows it. In contrast to the pseudo-trajectory, the shadowing trajectory cannot lie exactly on the unstable/stable manifolds $W^{\text{u/s}}(\Lambda)$, otherwise it would approach a neighborhood of Λ asymptotically and never leave it. However, the shadowing trajectory needs to be "close" to the unstable/stable manifolds if it has to pass close to the pseudo-trajectory. On the other hand, the shadowing trajectory should not be too close to $W^{\text{u/s}}(\Lambda)$ because then the transit time near Λ will be too large and therefore inefficient. The choice of a suitable proximity to unstable/stable manifolds $W^{\text{u/s}}(\Lambda)$ is a key point to achieve adequate shadowing trajectories. In practice, we want to use as much information from the pseudo-trajectory as possible to guide the search of the shadowing trajectory.

6. Multiple shooting.

Given the pseudo-trajectory $(\boldsymbol{Z}_i^-, \boldsymbol{Z}_{i+1}^+)_{i=1}^{N-1}$, we set up a *multiple shooting* scheme to find a shadowing trajectory. The method divides the interval over which the trajectory is sought into several smaller intervals, solves an initial value problem in each of the smaller intervals, and imposes additional matching conditions to form a solution on the whole interval.

Concretely, we look for points $(\boldsymbol{K}_i^-, \boldsymbol{K}_{i+1}^+)_{i=1}^{N-1}$ located *off* the unstable/stable manifolds,

$$\boldsymbol{K}_i^- = \boldsymbol{Z}_i^- + \Delta\boldsymbol{Z}_i^- = (\delta, y, I, \phi) \in \Sigma_-, \tag{6.1a}$$
$$\boldsymbol{K}_i^+ = \boldsymbol{Z}_i^+ + \Delta\boldsymbol{Z}_i^+ = (x, \delta, I, \phi) \in \Sigma_+, \tag{6.1b}$$

that satisfy the *matching conditions*

C.1 For every $i = 1, \dots, N-1$, there exist an intermediate point $\mathcal{K}$ in the global section $\mathscr{S} = \{Y = 0\}$ and an exterior time $T_{\text{ext}} = T_- + T_+$ such that

$$\boldsymbol{K}_i^- = \Phi_{-T_-}(\mathcal{K}) \qquad \text{and} \qquad \boldsymbol{K}_{i+1}^+ = \Phi_{T_+}(\mathcal{K}). \tag{6.2}$$

C.2 For every $i = 2, 3, \dots, N-1$, the forward trajectory of $\boldsymbol{K}_i^+ \in \Sigma_+$ matches the backward trajectory of $\boldsymbol{K}_i^- \in \Sigma_-$, i.e. there exists an interior time T_{int} within U such that

$$\Phi_{T_{\text{int}}}(\boldsymbol{K}_i^+) = \boldsymbol{K}_i^-. \tag{6.3}$$

Notice that the first integral $I_{\text{s}} = xy$ of the BNF is $x\delta$ in $\boldsymbol{K}_i^+$ and δy in $\boldsymbol{K}_i^-$. Thus, if Condition 2 is satisfied, then we must have $x = y$ in (6.1).

Together, these two conditions warrant $\Phi_{T_{\text{ext}}}(\boldsymbol{K}_i^-) = \boldsymbol{K}_{i+1}^+$ and $\Phi_{T_{\text{int}}}(\boldsymbol{K}_{i+1}^+) = \boldsymbol{K}_{i+1}^-$, so every point in $(\boldsymbol{K}_i^-, \boldsymbol{K}_{i+1}^+)_{i=1}^{N-1}$ belongs to one and the same trajectory. If the corrections $\Delta \boldsymbol{Z}_i^\pm$ turn out to be small, then the points $\boldsymbol{K}_\pm^i$ in the shadowing trajectory will be close to $\boldsymbol{Z}_i^\pm$ in the pseudo-trajectory. See Figure 2.

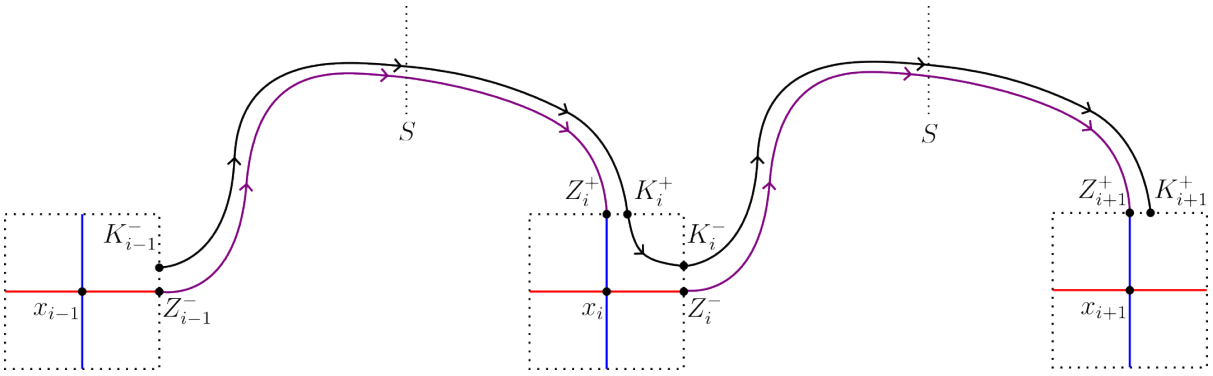


Figure 2: Schematic figure showing the pseudo-trajectory $(\boldsymbol{Z}_i^-, \boldsymbol{Z}_{i+1}^+)_i$, the corresponding chain of homoclinic trajectories (in purple), and a shadowing trajectory (in black). Condition 1 is verified on the Poincaré global section $\mathscr{S} = \{Y = 0\}$. See also Figure 13 for a numerical example of shadowing trajectory.

Remark 6.1. Figure 2 only shows a projection of the trajectories onto the saddle variables x, y. In fact, the action and angle variables I, ϕ must also match at the points $(\boldsymbol{K}_i^-, \boldsymbol{K}_{i+1}^+)_{i=1}^{N-1}$.

Typically, a modification of Newton's method is used to solve the system of equations (6.2) and (6.3).

We look for the unknown points $(\boldsymbol{K}_i^-, \boldsymbol{K}_{i+1}^+)_{i=1}^{N-1}$ in the boundary sections Σ_-, Σ_+, respectively. Thus, they are at the boundary ∂U of the normal form's domain (See Section 3). Numerically, this is very natural: Inside U, we use the integrable normal form to approximate the flow, thus avoiding the exponential growth of numerical errors due to hyperbolicity. (As shown in Section 8, within U the normal form is a very good approximation to the SR3BP flow.) Outside U, we integrate the flow numerically.

To improve numerical stability, close to Λ we always integrate the flow forward along the unstable manifold and backward along the stable manifold. Thus, it is natural to reformulate condition C.1 in the following way:

C.1' For every $i = 1, \dots, N-1$, there exists an intermediate point $\mathcal{K}$ in the global section $\mathscr{S} = \{Y = 0\}$ and times $T_\pm > 0$ such that

$$\Phi_{T_-}(\boldsymbol{K}_i^-) = \mathcal{K} = \Phi_{-T_+}(\boldsymbol{K}_{i+1}^+). \tag{6.4}$$

This condition is checked in the intermediate Poincaré global section $\mathscr{S}$, different from the boundary sections $\Sigma_\pm$.

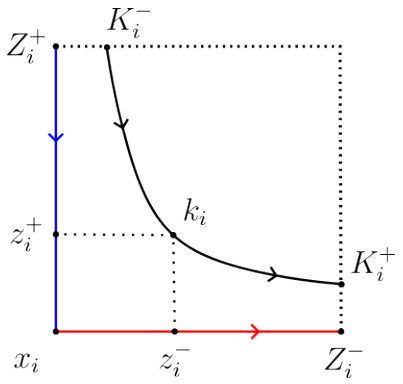


Figure 3: Construction of an initial guess for the multiple shooting procedure. $(\boldsymbol{k}_i)_i$ is an initial guess for shadowing the reduced pseudo-trajectory $(\boldsymbol{z}_i^-, \boldsymbol{z}_+^{i+1})_i$, whereas $(\boldsymbol{K}_i^-, \boldsymbol{K}_{i+1}^+)_i$ is an initial guess for shadowing the non-reduced pseudo-trajectory $(\boldsymbol{Z}_i^-, \boldsymbol{Z}_{i+1}^+)_i$.

We need to solve equations (6.3) and (6.4) for $(\boldsymbol{K}_i^-, \boldsymbol{K}_{i+1}^+)$. Notice that (6.3) consists of 5 equations in the boundary section Σ_-, and (6.4) consists of 5 equations in the global section $\mathscr{S}$. Condition C.1' amounts to $5(N-1)$ equations, while Condition C.2 amounts to $5(N-2)$ more. Thus, the total number of equations is $10N-15$. On the other hand, points $\boldsymbol{K}_i^-$ consist of 5 variables in the boundary section Σ_-, and $\boldsymbol{K}_{i+1}^+$ consist of 5 variables in the boundary section Σ_+. Thus, the total number of variables is $10N-10$. Hence, we may choose up to 5 extra conditions that the shadowing orbit must satisfy. In our computations, we fix some of the variables of the first and last point in the shadowing trajectory, namely the following (marked in boldface):

$$\begin{aligned} \boldsymbol{K}_1^- &= \left(\delta, \boldsymbol{y=0}, \boldsymbol{I_p = I_p^1}, \boldsymbol{I_v = I_v^1}, \phi\right) && \in W^{\mathrm{u}}(\Lambda_h) \cap \Sigma_-, \\ \boldsymbol{K}_N^+ &= \left(\boldsymbol{x=0}, \delta, I_{\mathrm{p}}, \boldsymbol{I_v = I_v^N}, \phi\right) && \in W^{\mathrm{s}}(\Lambda_h) \cap \Sigma_+. \end{aligned} \tag{6.5}$$

In this way, we impose that the shadowing trajectory tends to the first and last torus of the guiding orbit, with actions $I_{\mathrm{p}}^1, I_{\mathrm{v}}^1$ and I_{v}^N, as $t \to \pm\infty$ (see Equation (5.1)).

6.1. Initial guess. To solve the system of $10N-15$ equations given by (6.3) and (6.4), we need an initial guess of the unknown points $(\boldsymbol{K}_i^-, \boldsymbol{K}_{i+1}^+)_{i=1}^{N-1}$ in the boundary sections Σ_-, Σ_+. We cannot simply take $\boldsymbol{Z}_i^\pm$ as the initial guess for $\boldsymbol{K}_i^\pm$, because $\boldsymbol{Z}_i^\pm$ is exactly on the invariant manifold. Although $\boldsymbol{Z}_i^\pm$ satisfies condition C.1', it does not satisfy condition C.2. As explained in Section 5, the shadowing trajectory must be close to the invariant manifolds $W^{\mathrm{u/s}}(\Lambda_h)$, and the choice of an appropriate closeness is key. This means choosing the distance y from the point $\boldsymbol{K}_i^-$ to the unstable manifold $W^u(\Lambda_h)$ in Equation (6.1a), and the distance x from the point $\boldsymbol{K}_i^+$ to the stable manifold $W^s(\Lambda_h)$ in Equation (6.1b).

To obtain an appropriate initial guess, we will use the reduced pseudo-trajectory $(\boldsymbol{z}_i^-, \boldsymbol{z}_{i+1}^+)_i$. Recall from Remark 5.4 that $\left\|\boldsymbol{z}_i^+ - \boldsymbol{z}_i^-\right\| \le \delta$. For every $i = 2, 3, \dots, N-1$, consider the point $\boldsymbol{k}_i \in \Sigma$ defined as

$$\boldsymbol{k}_i = \left(x = \delta_-^i, y = \delta_+^i, I^i, \phi^i\right), \text{ with } I_{\mathrm{p}}^i = f_h(s_i, I_{\mathrm{v}}^i),\ \phi_{\mathrm{p}}^i = 0,$$

where $\delta_-^i, \delta_+^i, I^i, \phi^i$ are given in Equation (5.2), and $s_i = \delta_-^i\, \delta_+^i$. Notice that $\boldsymbol{k}_i$ and $\boldsymbol{z}_i^-$ differ only in the variable y, while $\boldsymbol{k}_i$ and $\boldsymbol{z}_i^+$ differ only in the variable x. See Figure 3.

Notice that $\boldsymbol{k}_i$ is δ-close to both $\boldsymbol{z}_i^+$ and $\boldsymbol{z}_i^-$, and is located off the unstable/stable manifolds. Moreover, the trajectory of $\boldsymbol{k}_i$ approaches the trajectory of $\boldsymbol{z}_i^+$ in backward time and that of

$\boldsymbol{z}_i^-$ in forward time,

$$\left\|\Phi_{-t}(\boldsymbol{k}_i) - \Phi_{-t}(\boldsymbol{z}_i^+)\right\| \le \exp(-t\lambda)\,\delta_+^i \quad \text{for } t \le t_-^i,$$
$$\left\|\Phi_{t}(\boldsymbol{k}_i) - \Phi_{t}(\boldsymbol{z}_i^-)\right\| \le \exp(-t\lambda)\,\delta_-^i \quad \text{for } t \le t_+^i.$$

Thus, $(\boldsymbol{k}_i)_i$ is a good initial guess for shadowing the reduced pseudo-trajectory.

Finally, we transport $\boldsymbol{k}_i$ to the boundary sections Σ_- and Σ_+ using the flow, in order to obtain an initial guess for shadowing the non-reduced pseudo-trajectory.

$$\boldsymbol{K}_i^- = \Phi_{t_-^i}(\boldsymbol{k}_i) \;\; = \left(x = \delta, y = s_i/\delta, I^i, \phi^i + t_-^i\nu\right) \in \Sigma_-,$$
$$\boldsymbol{K}_i^+ = \Phi_{-t_+^i}(\boldsymbol{k}_i) = \left(x = s_i/\delta, y = \delta, I^i, \phi^i - t_+^i\nu\right) \in \Sigma_+,$$

where $s_i = \delta_-^i\,\delta_+^i$, and ν is evaluated at $\boldsymbol{I} = (s_i, I^i)$.

Remark 6.2. Since $s_i = \delta_-^i\delta_+^i \neq 0$, the time $t_\pm^i = t_\pm^i(s_i, I^i)$ and frequency $\nu = \nu(s_i, I^i)$ used here is different from the time $t_\pm^i = t_\pm^i(0, I^i)$ and frequency $\nu = \nu(0, I^i)$ used for $s = 0$ in (5.3): $t_\pm^i(s_i, I^i) = (1 + O(s_i))t_\pm^i(0, I^i)$, so $\boldsymbol{K}_i^-$ and $\boldsymbol{Z}_i^-$ differ not only in coordinate y, but also slightly in ϕ.

Therefore, the sequence $(\boldsymbol{K}_i^-, \boldsymbol{K}_{i+1}^+)_i$ is an initial guess to shadow the pseudo-trajectory $(\boldsymbol{Z}_i^-, \boldsymbol{Z}_{i+1}^+)_i$. The initial guess constructed $(\boldsymbol{K}_i^-, \boldsymbol{K}_{i+1}^+)_i$ **satisfies condition C.2** but does not exactly satisfy C.1'. However, in practice, this initial guess is close enough to the solution of the multiple shooting method, and we will see that the method converges (Section 9.3).

7. Analytical error estimates for the Sun–Earth BNF.

Proposition 8.1 in the paper [8] gives bounds for the norm of the normal form and its reminder. In this section, we compute these theoretical bounds for L_1 in the Sun-Earth SR3BP.

As the Hamiltonian H (3.1) is analytic for $\varepsilon < 1$, one can expect $\|H_s\| \le c^{s-2}d$, $s \ge 2$ only for $c \ge 1$ in the original coordinates. Taking into account the linear symplectic change (3.2), in the coordinates (x, y) we obtain $\|H_s\| \le c^{s-2}d$, with $c = 2.09$ and $d = \|H_2\| = \lambda^0 + \nu_{\mathrm{p}}^0 + \nu_{\mathrm{v}}^0 = 6.63$. Indeed, we have numerically computed the norm of all homogeneous polynomials H_s up to order 32, see Figure 4. The value $c = 2.09$ is obtained by fitting the function $c^{s-2}d$ to these numerical data. Other theoretical estimates can be found in [10].

For our numerical computations, we have implemented a BNF of order $M = 16$. This choice requires computing the small divisors $\alpha_3 \ge \alpha_4 \ge \cdots \ge \alpha_{16}$ given in equation (3.3) for the Sun-Earth mass ratio $\mu_{\text{Sun-Earth}} = 3.040423398444176 \cdot 10^{-6}$. In this system, c_2 takes the value $c_2 = 4.061074016255354$, and $\lambda^0 = 2.532659174052968$, $\nu_{\mathrm{p}}^0 = 2.086453564223108$, $\nu_{\mathrm{v}}^0 = 2.015210662996639$.

The frequency ratio $\omega^0 := \nu_{\mathrm{v}}^0/\nu_{\mathrm{p}}^0 = 0.9658545474253123$ can be expressed by the continued fraction expansion:

$$\omega^0 = 1 + \cfrac{1}{-29 + \cfrac{1}{-3 + \cfrac{1}{-2}}}$$

Consequently, the resonance order of ω^0 is approximately $\operatorname{round}\left(\frac{1}{1-\omega^0}\right) = 29$. This implies that $28/29$ is a remarkably close rational approximation of ω^0, with a residual of $\omega^0 - 28/29 = 0.00033730604$, and there is no better rational approximation with a denominator smaller than 29.

Evaluating the small divisors (3.3) reveals that:

$$\alpha(3) = \cdots = \alpha(26) = 0.21372870367940491,$$
$$\alpha(27) = 0.16289523110846341,$$
$$\alpha(28) = 0.091652329881995109,$$
$$\alpha(29) = 0.020409428655526807.$$

Thus, the divisors $\alpha(s)$ remain stable at approximately 0.21 up to the order 26, where the Birkhoff normal form (BNF) remains highly reliable. However, at order 29, they drop significantly to 0.02. This drop indicates that a less restrictive normal form, such as the Birkhoff–Gustavson Normal Form (BGNF), would provide greater reliability and better capture resonant effects for larger action values, including those corresponding to halo orbits.

Finally, plugging the radius $r = r_{16} = 2.8303 \cdot 10^{-5}$ into [8, Equation (8.3)] yields an error $\left|\mathcal{R}^{(16)}\right|_r \leq \epsilon_{16} = 3.57 \cdot 10^{-7}$ for the BNF remainder. Although this error is reasonably small, the underlying theoretical bounds demand an extremely restrictive radius of applicability. In the next section, we compare this analytical prediction with direct numerical estimates of the actual validity radius of the BNF.

8. Numerical error estimates for the Sun–Earth BNF. In this section, we consider the SR3BP and numerically compute its BNF up to order $M = 16$. In this way, we can explicitly compute the norms $\|\mathcal{Z}_s\|, \|\mathcal{R}_s\|$ and compare them with their theoretical bounds.

First, we expand the Hamiltonian (3.1) up to order 32 and apply the diagonalizing change of coordinates (3.2), obtaining

$$H(Q,P) = \sum_{s=2}^{32} H_s(Q,P).$$

The size of each term $\|H_s\|$ is shown in Figure 4. Fitting the bound $c^{s-2}d$ to these data allows us to obtain the constants $c = 2.09$ and $d = 6.63$.

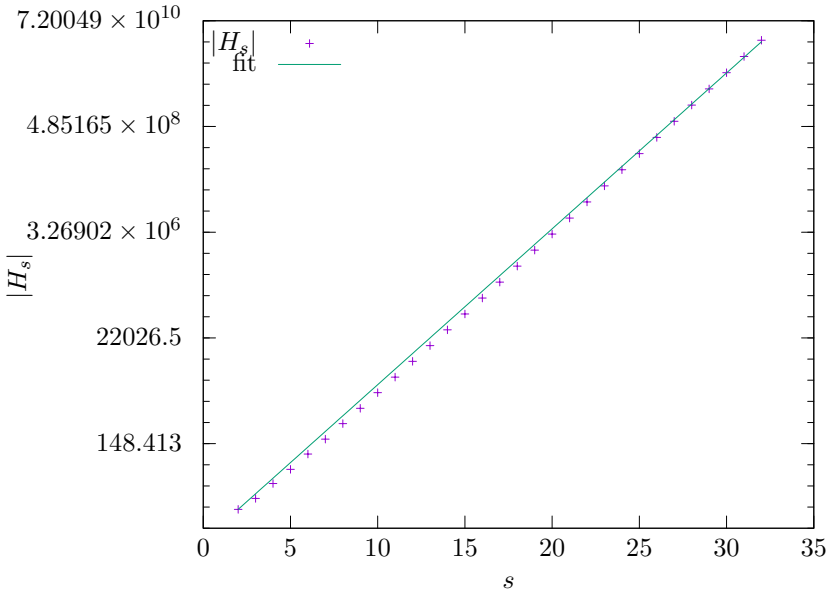


Figure 4: Numerically computed values of $\|H_s\|$, and their fit $c^{s-2}d$. The vertical axis is plotted in logarithmic scale.

Then, we compute its normal form up to order $M = 16$, namely,

$$\mathcal{H}^{(16)} = H_2 + \mathcal{Z}^{(16)}(\boldsymbol{I}) + \mathcal{R}^{(16)}(q,p),$$

with

$$\mathcal{Z}^{(16)}(\boldsymbol{I}) = \sum_{\substack{s \text{ even} \\ 4 \leq s \leq 16}} \mathcal{Z}_s(\boldsymbol{I}), \quad \mathcal{R}^{(16)}(q,p) = \sum_{s=17}^{32} \mathcal{R}_s^{(16)}(q,p).$$

The size of each homogeneous polynomial $\|\mathcal{Z}_s\|$ and $\|\mathcal{R}_s\|$ is shown in Figure 5.

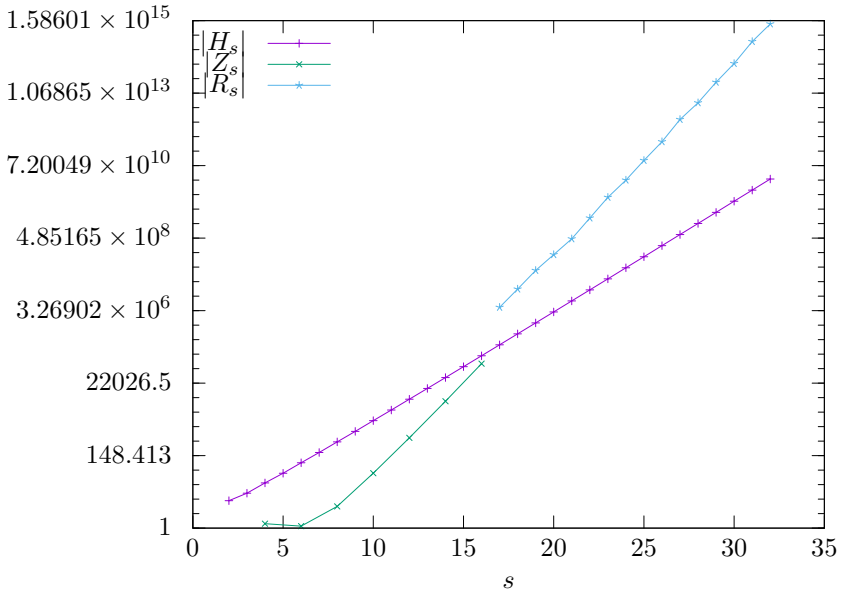


Figure 5: Numerically computed values of $\|\mathcal{Z}_s\|$ and $\|\mathcal{R}_s\|$, compared to $\|H_s\|$. The vertical axis is plotted in logarithmic scale.

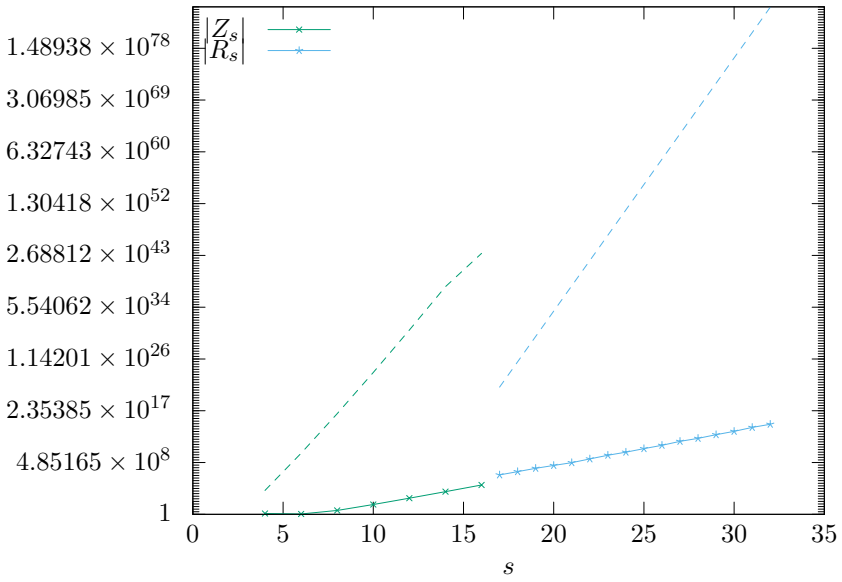


Figure 6: Numerically computed values of $\|\mathcal{Z}_s\|$ and $\|\mathcal{R}_s\|$, compared to their theoretical bounds (dashed lines). The vertical axis is plotted in logarithmic scale.

One can also compare $\|\mathcal{Z}_s\|$ and $\|\mathcal{R}_s\|$ with their theoretical bounds, given in [8, Proposition 8.1]. For the theoretical bounds, we have used the value $a = 20$, the numerically fitted coefficients $c = 2.09$ and $d = 6.63$, as well as the small divisors $\alpha(3) = \cdots = \alpha(16) = 0.21372870367940491$. Figure 6 compares $\|\mathcal{Z}_s\|$ and $\|\mathcal{R}_s\|$ with their theoretical bounds. Clearly, the theoretical bounds are very conservative.

To complement the theoretical estimates of the error in the normal form, derived in Section 7, we will now measure this error more precisely using semi-analytical methods. Specifically, we will look for the domain of validity U of the computed normal form transformation $\mathcal{K} = \Psi(\boldsymbol{Z})$,

which is used to parameterize all points close to the NHIM Λ. Recall from Section 3 that

$$\Lambda = W^{\mathrm{c}}_{\mathrm{loc}} = \{\boldsymbol{X} = (x = 0, y = 0, I, \phi)\} = \{(0,0)\} \times [0, r]^2 \times \mathbb{T}^2$$

is the local center manifold of L_1 for the normal form system, which is a 4-dimensional NHIM.

For points $\boldsymbol{Z}$ located either in Λ or in the stable manifold $W^{\mathrm{s}}(\Lambda)$, we define the *error in the orbit of* $\boldsymbol{Z}$

$$\epsilon(\boldsymbol{Z}) = \sup_{t\in[0,T=3]} \|\Psi(\Phi_t(\boldsymbol{Z})) - \Phi_t(\Psi(\boldsymbol{Z}))\|.$$

In the first term, $\Phi_t(\boldsymbol{Z})$ is computed exactly using Equation (3.5). In the second term, $\Phi_t(\Psi(\boldsymbol{Z}))$ is computed using numerical integration, more specifically a Runge-Kutta Prince-Dormand (8, 9) method with local error 10^{-16}.

Remark 8.1. The orbit error of $\boldsymbol{Z}$ is calculated over a time span of $T = 3$ units because this is the approximate period of vertical and horizontal oscillations of solutions around the equilibrium point.

For ease of visualization, we will summarize the orbit error over all horizontal angles ϕ_{p}. Let $\boldsymbol{Z} = (x, y, I, \phi) \in U$, and define its *maximal orbit error over* ϕ_{p}

$$\bar{\epsilon}(\boldsymbol{Z}) = \sup_{\phi_{\mathrm{p}}\in[0,2\pi]} \epsilon(\boldsymbol{Z}).$$

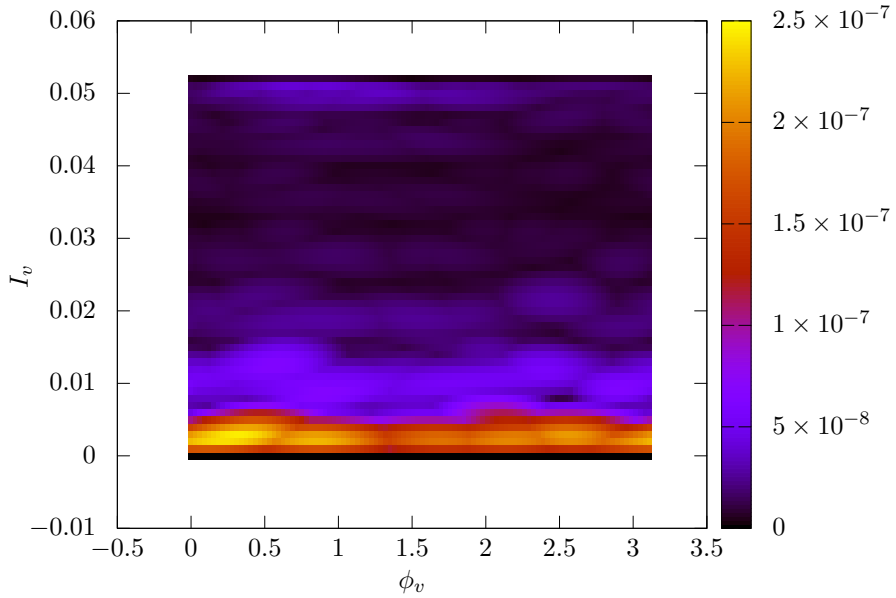


Figure 7: Maximal orbit error $\bar{\epsilon}(\boldsymbol{X})$ of points $\boldsymbol{X} = (0, 0, I, \phi) \in \Lambda_h$ as a function of $I_{\mathrm{v}}, \phi_{\mathrm{v}}$.

First, we compute the error on the NHIM Λ_h of energy value $h = -1.50044$ (Jacobi constant $C = 3.00088$). For each point $\boldsymbol{X} \in \Lambda_h$, we compute its maximal orbit error using a normal form of order $M = 16$. See Figure 7.

Then, we compute the error on the stable manifold $W^{\mathrm{s}}(\Lambda_h)$. The maximal orbit error is computed for each point $\boldsymbol{Z} = (0, \delta, I, \phi) \in W^{\mathrm{s}}(\Lambda_h)$ located at a distance δ from the NHIM along its stable fiber. See Figure 8. This experiment is repeated for several values of δ in order to determine the domain of validity of the normal form of order 16 to represent the stable manifold. Figure 8 shows that the stable manifold can be extended to $\delta = 0.1$ without significantly affecting the orbit error. Similar results are obtained for the unstable manifold, integrating backwards over a time span of $T = -3$ time units.

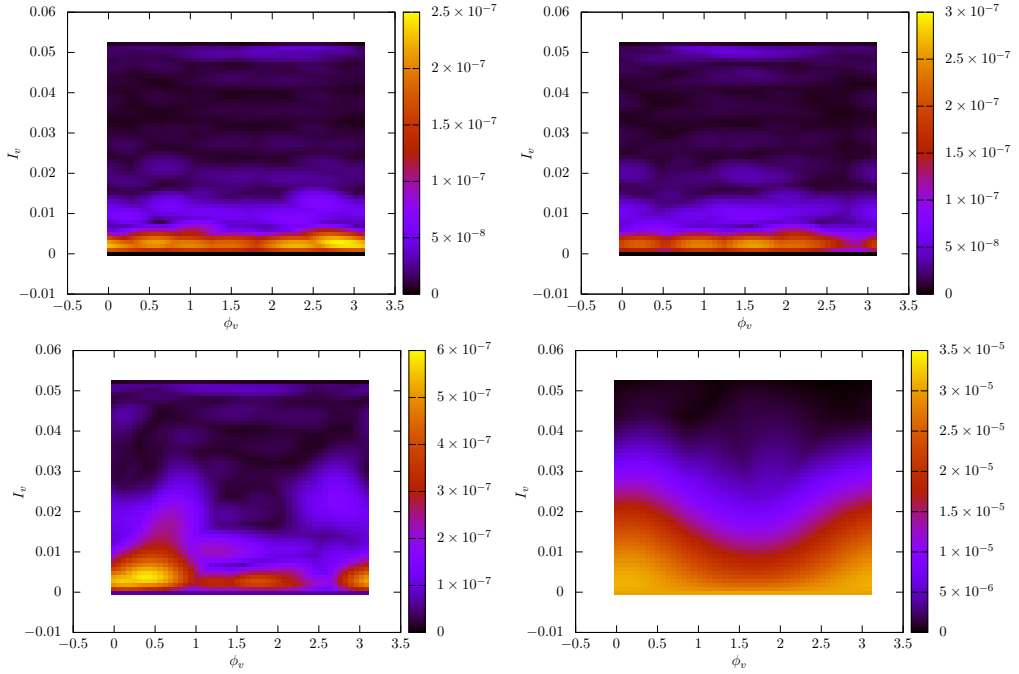


Figure 8: Maximal orbit error $\bar{\epsilon}(\boldsymbol{Z})$ of points $\boldsymbol{Z} = (0, \delta, I, \phi) \in W^{\mathrm{s}}(\Lambda_c)$ for several values $\delta = 0.001, 0.1, 0.25, 0.5$. Similar results are obtained for the unstable manifold.

Finally, we compute the error in $U = [-\delta, \delta]^2 \times [0, r]^2 \times \mathbb{T}^2$, *away* from the invariant manifolds. In this case, it is not guaranteed that $\Phi_t(\boldsymbol{Z})$ will stay in the neighborhood U for all $t \in [0, 3]$. In particular, the unstable x-component grows exponentially, so it can escape $[-\delta, \delta]$. Thus, we slightly modify the definition of the error in the orbit of $\boldsymbol{Z}$. Let $\boldsymbol{Z} = (x, y, I, \phi) \in U$ with $0 < x < \delta$, and define

$$\epsilon(\boldsymbol{Z}) = \sup_{t \in [0,T]} \|\Psi(\Phi_t(\boldsymbol{Z})) - \Phi_t(\Psi(\boldsymbol{Z}))\| \qquad \text{with } T = \min\{T_{\mathrm{exit}}, 3\},$$

where $T_{\mathrm{exit}}(\boldsymbol{Z})$ is the time to exit U, that is, $\Phi_{T_{\mathrm{exit}}}(\boldsymbol{Z}) \in \partial U$. We summarize the orbit error over all actions I and angles ϕ. Let $\boldsymbol{Z} = (x, y, I, \phi) \in U_c$ be a point with energy value $C = c$, and define

$$\bar{\epsilon}(x, y) = \sup_{I \in [0,r]^2, \phi \in [0, 2\pi]^2} \epsilon((x, y, I, \phi)).$$

For each point $\boldsymbol{Z} \in U_c$, we compute its maximal orbit error $\bar{\epsilon}(x, y)$ using a normal form of order $M = 16$. See Figure 9. This figure shows that the neighborhood U_c can be extended to $\delta = 0.1$ without significantly affecting the orbit error, which remains smaller than 3×10^{-7}.

9. Semi-analytical results.

9.1. Series representation of the reduced transition maps. Consider the saddle-center-center equilibrium point L_1 of the spatial restricted three-body problem (SR3BP). The Birkhoff normal form (BNF) introduced in Section 3 can be used to approximate the flow of the SR3BP in a neighborhood of L_1 (see [12, 7, 9]). Fix the degree $M = 16$ of the normal form and the energy value $h = -1.50044$ (Jacobi constant $C = 3.00088$).

Recall that the normal form is computed in a neighborhood $U(\delta, r) = [-\delta, \delta]^2 \times [0, r]^2 \times \mathbb{T}^2$. As explained in [8, Remark 5.6], the transition maps depend on the choice of δ. To explore this dependence, we will consider two neighborhoods, a smaller $U(\delta = 0.001, r = 0.05)$ and a larger $U(\delta = 0.1, r = 0.05)$. The normal form provides an excellent approximation of the flow in both neighborhoods. As shown in Section 8, the maximal orbit error is 2.5×10^{-7}.

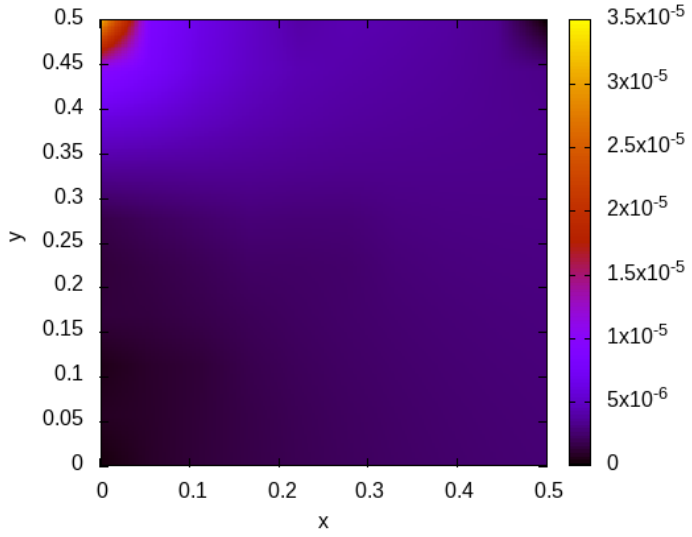


Figure 9: Maximal orbit error $\bar{\epsilon}(x, y)$ of points $\boldsymbol{Z} = (x, y, I, \phi) \in U$ as a function of x, y.

Notation change: Starting with this section, we rescale the action and write (J, ϕ) instead of $(1000\, I_{\rm v}, \phi_{\rm v})$.

We consider the annulus $\mathcal{A} \subset \Lambda_h^\Sigma$ given by

$$\mathcal{A} = \{(J, \phi) \colon \ J \in [1, 7] \text{ and } \phi \in [0, 2\pi)\}.$$

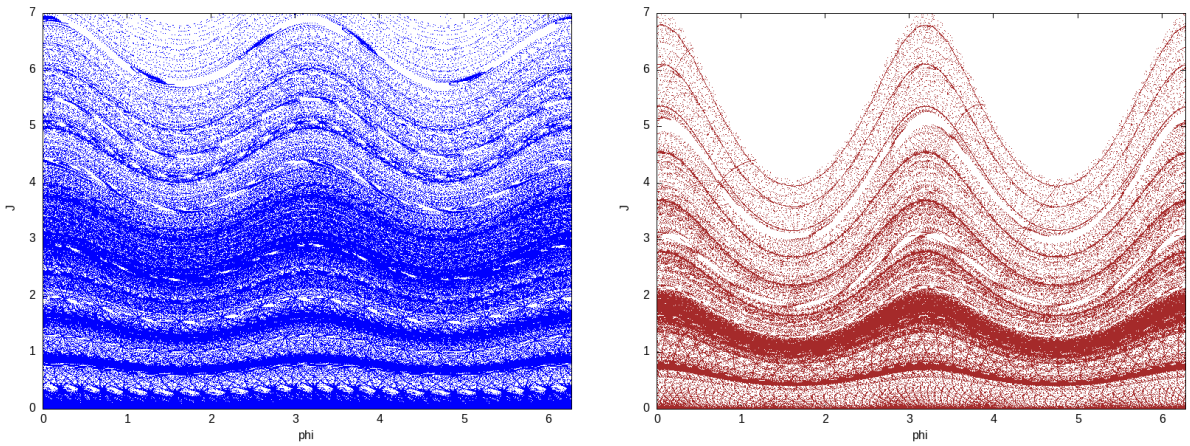
Using the techniques developed in [9], we compute two transition maps $\tau_{1,2}$ on $\mathcal{A}$. More precisely, we start by computing the transition maps on a few invariant tori $J = 1, \dots, 7$. Then we compute a (Fourier-Polynomial) series representation of $\tau_{1,2}$. After that, we can apply the transition maps to any point (J, ϕ) in their domain $\mathcal{A}$, that is, $(J', \phi') = \tau_{1,2}(J, \phi)$. Figure 10 shows the global phase portraits of $\tau_{1,2}$, obtained by taking a grid of 300×300 initial conditions evenly distributed in the domain $\mathcal{A}$ and iterating each initial condition 100 times. See [9] for a detailed analysis of the phase portraits. Some comments are in order:

- The dependence of $\tau_{1,2}$ on the size δ of the normal form neighborhood U is very small. However, this small difference has dramatic consequences for the phase portraits, such as the size and location of the main resonances (see Figure 10). It also has dramatic consequences for the shortest-time guiding orbit, as we shall see in Section 9.2.
- τ_2 allows for larger "jumps" in terms of action J than τ_1. However, we will show that the shortest-time guiding orbit uses both τ_1 and τ_2.
- The J-component of $\tau_{1,2}$ is a π-periodic function of the angle, as seen in Figure 10 and proved in [9]. However, the ϕ-component is not.

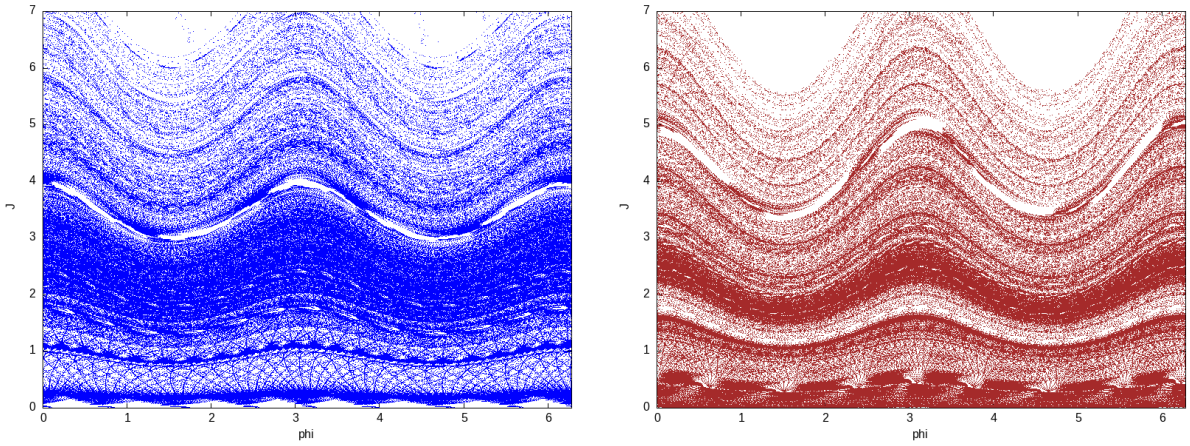
9.2. Shortest-time drift guiding orbit. Let $f \colon \Lambda_h^\Sigma \to \Lambda_h^\Sigma$ be the inner map given by $J' = J$, $\phi' = \phi + \omega(J)$. In terms of the inner flow of the SR3BP, an application of the inner map corresponds to integrating an initial condition $(J_v, \phi_p = 0, \phi_v) \in \Lambda_h^\Sigma$ during the amount of time it takes to return to the global section Σ within U. Thus, each iterate of the inner map takes time $t_{\rm in} = 2\pi/\nu_p(J)$. Numerically, we find that $2.0764 < \nu_p(J) < 2.0781$, and therefore the inner time is bounded by

$$3.0235 < t_{\rm in} < 3.0261.$$

In terms of SR3BP flow, one application of the transition map corresponds to a (segment of) a homoclinic trajectory from $\boldsymbol{z}_- \in W^u(\Lambda_h^\Sigma)$ to $\boldsymbol{z}_+ \in W^s(\Lambda_h^\Sigma)$. The transition time $t_{\rm out}$



(a) $\tau_1(\delta = 0.1)$ (b) $\tau_2(\delta = 0.1)$



(c) $\tau_1(\delta = 0.001)$ (d) $\tau_2(\delta = 0.001)$

Figure 10: Phase portrait of the reduced transition maps τ_1 (left) and τ_2 (right) when $\delta = 0.1$ (top) and $\delta = 0.001$ (bottom).

from $\boldsymbol{z}_-$ to $\boldsymbol{z}_+$ depends on the size δ of the neighborhood U and on the transition map (τ_1 or τ_2). Of course, it also depends on the particular homoclinic, but this dependence is quite mild. We have computed the transition time t_{out} for all homoclinics starting on the invariant tori $J = 1, 2, \ldots, 7$. The results are shown in Table 1.

	τ_1	τ_2
$\delta = 0.1$	$5.45 \leq t_{\text{out}} \leq 5.71$	$4.95 \leq t_{\text{out}} \leq 5.21$
$\delta = 0.001$	$8.32 \leq t_{\text{out}} \leq 8.52$	$8.00 \leq t_{\text{out}} \leq 8.21$

Table 1: Transition times t_{out}.

Notice that enlarging the neighborhood U by two orders of magnitude (from $\delta = 0.001$ to $\delta = 0.1$) considerably reduces t_{out}, which then becomes less than twice the inner time t_{in}.

In [9], we introduced different algorithms to produce *drift guiding orbits*, that is, orbits of the iterated function system (IFS) $\{f, \tau_1, \tau_2\}$ consisting of the inner map f and transition maps $\tau_{1,2}$, whose action variable J increases from $J = 1$ to $J > 7$. Using the previous time estimates,

we can estimate the *total drift time* of the guiding orbit as

$$t = n_0 t_{\text{in}} + n_1 t_{\text{out}} + n_2 t_{\text{out}},$$

where n_0, n_1 and n_2 denote the number of iterations of f, τ_1 and τ_2, respectively. In particular, the Shortest-Time Algorithm ([9], Section 12.2) looks for a drift guiding orbit with the shortest total time.

Consider first the case $\delta = 0.1$, with an IFS $\{f, \tau_1(\delta = 0.1), \tau_2(\delta = 0.1)\}$. In this case, the Shortest-Time Algorithm produces the guiding orbit of Figure 11a with a total drift time 121.3 in normalized time units, equivalent to 19.3 years. Consider next the case $\delta = 0.001$, with an IFS $\{f, \tau_1(\delta = 0.001), \tau_2(\delta = 0.001)\}$. In this case, the Shortest-Time Algorithm produces the guiding orbit of Figure 11b with a total drift time 220.2, or 35 years.

The resulting guiding orbits are strikingly different in each case. When $\delta = 0.001$, it uses all three maps f, τ_1, τ_2. In particular, the guiding orbit uses the inner map f repeatedly to decrease the angle ϕ until it reaches a location where $\tau_{1,2}$ can be applied to increase action J.

In contrast, when $\delta = 0.1$, the shortest-time orbit does not use the inner map at all: it only uses τ_1 and τ_2. Recall that τ_2 makes larger "jumps" in terms of action than τ_1. The algorithm manages to find a path where τ_2 is applied often, always to increase the action, even at the expense of applying τ_1 too, always to *decrease* the action but not as much.

Another factor that explains the qualitative difference between the shortest-time orbits is the ratio between the inner time t_{in} and the transition time t_{out}. When $\delta = 0.001$, t_{out} is much larger than t_{in}, so $\tau_{1,2}$ are used sparingly. When $\delta = 0.1$, t_{out} is not much larger than t_{in}, so $\tau_{1,2}$ can be used more often.

Lemma 2.6 and Theorem 3.1 in [8] give conditions that guarantee that such guiding orbits can be shadowed by true orbits. While these are general theoretical results that guarantee the existence of shadowing orbits under some conditions, the multiple shooting scheme presented in Section 6 provides the explicit numerical construction of such shadowing orbits.

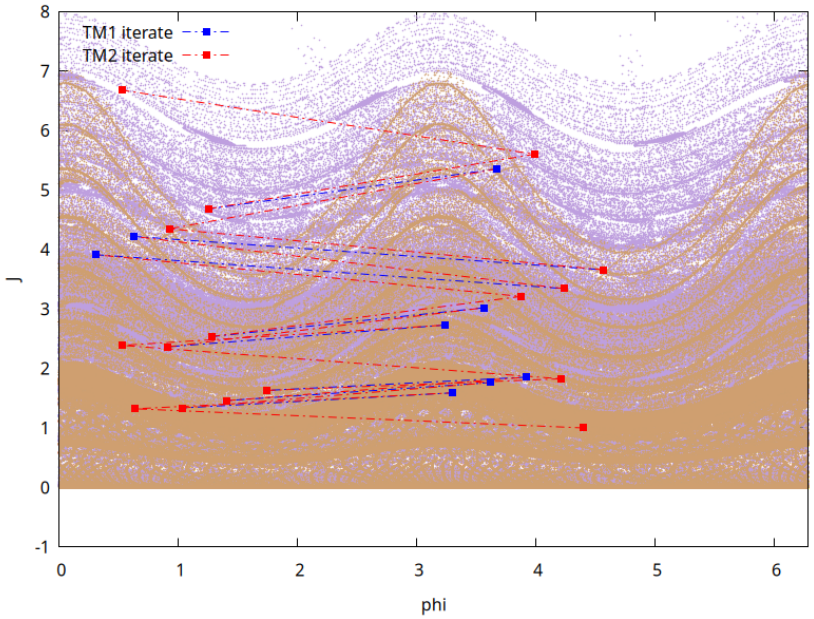
Remark 9.1. The scattering map cannot be used to design optimal time guiding orbits. It is defined through asymptotic homoclinics, so it does not carry any information on time. In this situation, it is necessary to use the transition map.

9.3. Shadowing trajectory. Consider the case $\delta = 0.1$. Let the guiding orbit consist of the last $N = 17$ iterates of the shortest-time drift orbit given in Figure 11a, starting at $\boldsymbol{x}_1 = (\phi, J) = (1.743404, 1.630975)$ and ending at $\boldsymbol{x}_{17} = (\phi, J) = (6.677670, 0.528935)$. Each iterate in the guiding orbit $\{\boldsymbol{x}_i \in \Lambda_h^\Sigma\}_{i=1,\dots,N}$ satisfies either $\tau_1(\boldsymbol{x}_i) = \boldsymbol{x}_{i+1}$ or $\tau_2(\boldsymbol{x}_i) = \boldsymbol{x}_{i+1}$. Our goal is to shadow this guiding orbit using the method of Section 6.

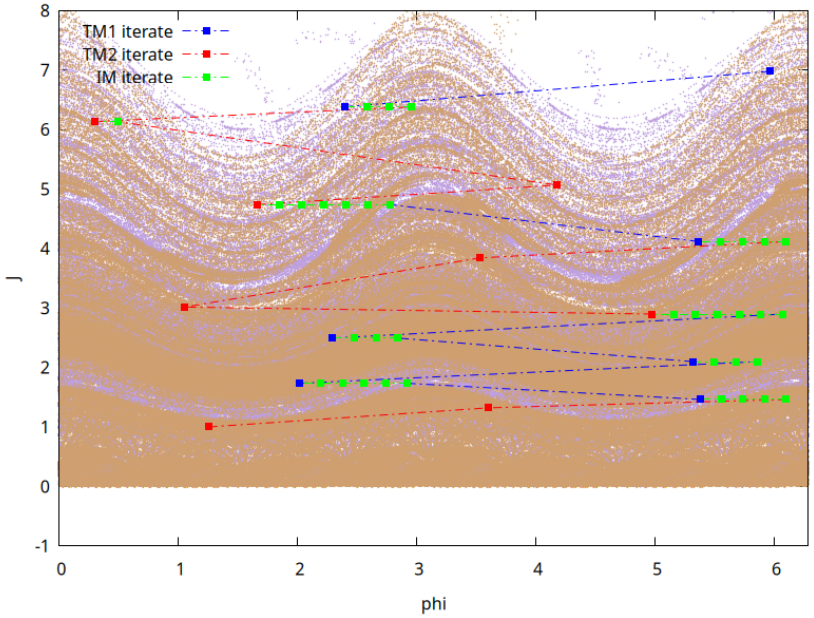
To this guiding orbit, we associate a sequence of $N - 1 = 16$ Λ_h-homoclinic trajectory segments. When the segments end at the boundary ∂U of the normal form domain, the endpoints $(\boldsymbol{Z}_i^-, \boldsymbol{Z}_{i+1}^+)_{i=1}^{N-1}$ make up the pseudo-trajectory. If the segments are further extended to the global section $\Sigma = \{\phi_{p,\pm} = 0\}$ within U, then the endpoints $(\boldsymbol{z}_i^-, \boldsymbol{z}_{i+1}^+)_{i=1}^{N-1}$ make up the reduced pseudo-trajectory. See Figure 12. This reduced pseudo-trajectory has a total drift time 83.5896 adimensional time units, or 13.3 years.

As explained in Remark 5.4, the reduced pseudo-trajectory determines a pseudo-orbit in the classical sense [3], that is, the last point of each trajectory segment is close to the first point of the next segment. This is clear in Figure 12b: there are small (but visible) gaps between consecutive segments, gaps located around $(X = -0.99, Y = 0.004)$. See a closeup of the gaps in Figure 14.

The error of this pseudo-trajectory can be estimated as the total size of these gaps. Let $\boldsymbol{z}_i^+ = (x_i^+, v_i^+)$ denote the last point of a segment in position-velocity coordinates, and $\boldsymbol{z}_i^- = (x_i^-, v_i^-)$ the first point of the next segment. Each of these gaps has an average position error $\|\Delta x_i\| = \left\|x_i^+ - x_i^-\right\| \approx 8.2 \times 10^{-5}$ adimensional units, and an average velocity error $\|\Delta v_i\| = \left\|v_i^+ - v_i^-\right\| \approx 2.1 \times 10^{-4}$ adimensional units. Since there are 15 gaps, the total position error is



(a) $\delta = 0.1$. Total drift time 121.3.

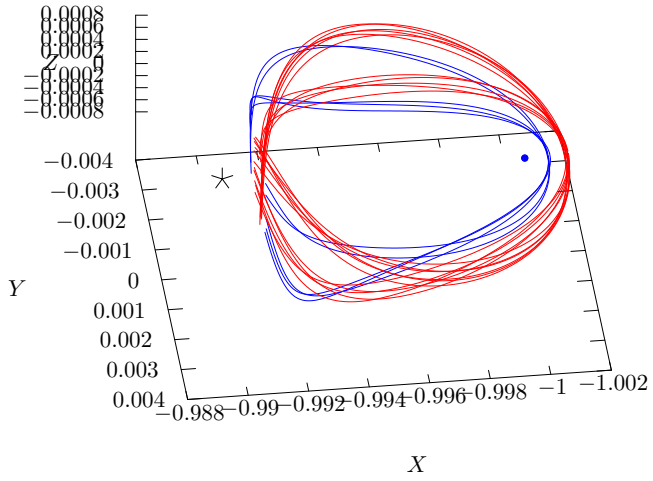


(b) $\delta = 0.001$. Total drift time 220.2.

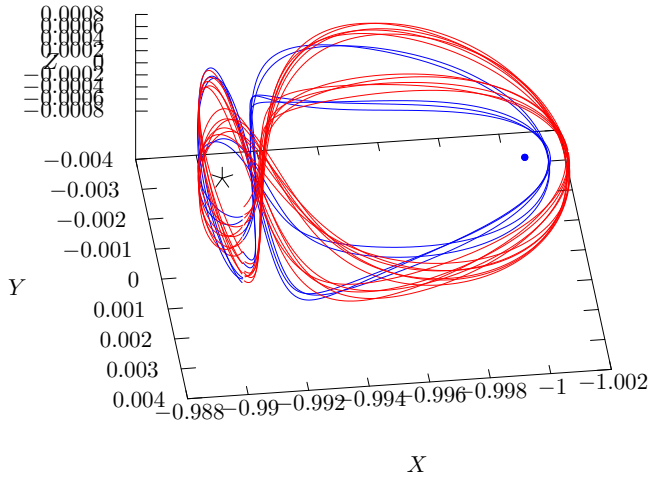
Figure 11: Shortest-time drift orbit found by iterating the triple dynamical system $\{f, \tau_1, \tau_2\}$ when $\delta = 0.1$ (above) and $\delta = 0.001$ (below). A point x_i in the orbit is plotted in blue if $\tau_1(x_i) = x_{i+1}$, red if $\tau_2(x_i) = x_{i+1}$, and green if $f(x_i) = x_{i+1}$. Consecutive iterates are joined by dashed segments to help visualize the orbit.

$\|\Delta x\| = 1.23 \times 10^{-3}$, and total velocity error $\|\Delta v\| = 3.15 \times 10^{-3}$. In the Sun-Earth system, the adimensional length unit corresponds to 1 AU (Astronomical Unit) $= 1\,496 \times 10^8$ km, while 2π adimensional time units correspond to 1 year. Therefore, the total position and velocity errors amount to $\|\Delta x\| = 184\,005$ km and $\|\Delta v\| = 338\,000$ km/h $= 93.89$ km/s.

Finally, we apply the multiple shooting method described in Section 6. We look for



(a) Homoclinic trajectory segments ending on the pseudo-trajectory $(\boldsymbol{Z}_i^-, \boldsymbol{Z}_{i+1}^+)_{i=1}^{N-1}$



(b) Homoclinic segments ending on the reduced pseudo-trajectory $\{(\boldsymbol{z}_-^i, \boldsymbol{z}_+^{i+1})\}_{i=1}^{N-1}$

Figure 12: Sequence of $N-1=16$ homoclinic trajectory segments (in original SR3BP coordinates) associated to the guiding orbit. Blue segments are associated to the transition map τ_1, red segments to τ_2. The Earth location is marked by the blue circle, while the equilibrium point L_1 is marked by a black star.

$2(N-1) = 32$ points $(\boldsymbol{K}_i^-, \boldsymbol{K}_{i+1}^+)_{i=1}^{N-1}$ in the boundary sections $\Sigma_\pm$ that satisfy the matching conditions C.1' and C.2. This corresponds to solving the system of equations (6.4), (6.3) and (6.5), consisting of $10N-10=160$ real equations in $10N-10=160$ variables. We use the multidimensional Newton's method to solve the system.

Since the shadowing trajectory is hyperbolic and thus unstable, this requires the initial guess to be very close to an actual but unknown trajectory. Indeed, we have used the initial guess proposed in Section 6.1.

A root of Newton's method is found with absolute error 10^{-12}. This implies that the total position and velocity error of the shadowing trajectory is within 10^{-12}; that is, $\|\Delta x\| < 10^{-12}$, $\|\Delta v\| < 10^{-12}$. In physical units, this amounts to $\|\Delta x\| < 1.49598$ m and $\|\Delta v\| < 2.9806 \times 10^{-5}$ m/s. Compare these errors to those of the differential correction method used in Section 10 (29 m and 0.006 m/s). Clearly, the multiple-shooting method produces a more precise shadowing trajectory.

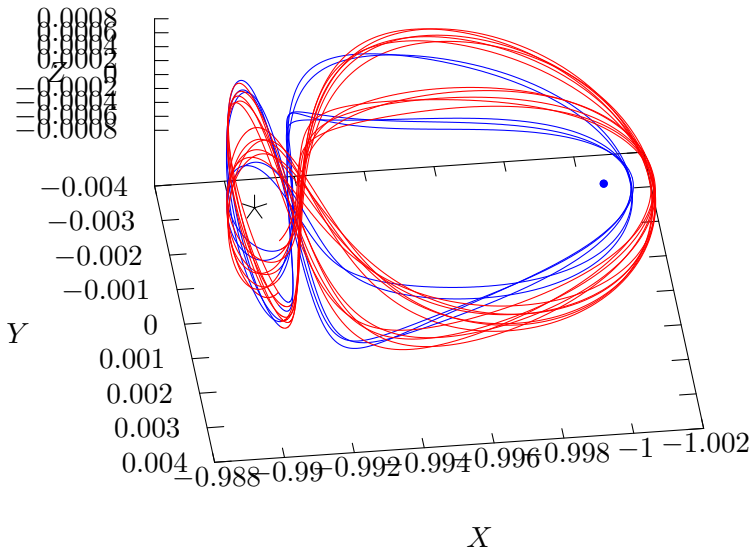


Figure 13: Shadowing trajectory corresponding to the pseudo-trajectory of Figure 12. The small gaps that were present in the pseudo-trajectory have been closed.

The resulting shadowing trajectory is shown in Figure 13. Notice that the small gaps present in the pseudo-trajectory 12 have been closed. The shadowing trajectory has a total drift time 83.5874, which is very similar to that of the pseudo-trajectory.

x	y	I_{p}	I_{v}	ϕ_{p}	ϕ_{v}	t_+	T_{int}	$t_+ + \frac{2\pi}{\nu_{\mathrm{v}}}$
1.209337e-04	-1.000000e-01	4.836035e-02	2.003625e-03	5.065988e+00	2.829394e+00	1.655701e+00	2.652066e+00	4.667774e+00
1.202584e-04	-1.000000e-01	4.782276e-02	2.557167e-03	5.064408e+00	5.473926e+00	3.879481e-01	2.654277e+00	3.400022e+00
4.869715e-05	-1.000000e-01	4.765769e-02	2.718287e-03	5.066777e+00	1.912417e+00	2.095287e+00	3.011174e+00	5.107360e+00
4.833341e-05	-1.000000e-01	4.792152e-02	2.446521e-03	4.313133e+00	5.124596e+00	5.554119e-01	3.014134e+00	3.567485e+00
4.881234e-05	-1.000000e-01	4.736196e-02	3.022895e-03	5.056019e+00	2.243910e+00	1.936374e+00	3.010242e+00	4.948447e+00
4.815479e-05	-1.000000e-01	4.782672e-02	2.544133e-03	4.322214e+00	5.506668e+00	3.722520e-01	3.015596e+00	3.384326e+00
1.142642e-04	-1.000000e-01	4.712836e-02	3.271653e-03	5.041091e+00	2.545108e+00	1.791984e+00	2.674462e+00	4.804057e+00
4.897135e-05	-1.000000e-01	4.657093e-02	3.837777e-03	5.040550e+00	5.271619e+00	4.849309e-01	3.008958e+00	3.497004e+00
4.814316e-05	-1.000000e-01	4.707655e-02	3.316801e-03	4.338323e+00	2.231280e+00	1.942428e+00	3.015691e+00	4.954502e+00
4.903114e-05	-1.000000e-01	4.623255e-02	4.186421e-03	5.021040e+00	5.580117e+00	3.370415e-01	3.008476e+00	3.349115e+00
4.798710e-05	-1.000000e-01	4.681267e-02	3.588618e-03	4.356312e+00	2.590640e+00	1.770156e+00	3.016973e+00	4.782229e+00
1.040047e-04	-1.000000e-01	4.604983e-02	4.381515e-03	5.000651e+00	5.869450e+00	1.983390e-01	2.711603e+00	3.210412e+00
4.936078e-05	-1.000000e-01	4.511055e-02	5.342652e-03	4.993494e+00	2.334512e+00	1.892940e+00	3.005831e+00	4.905014e+00
4.783102e-05	-1.000000e-01	4.577267e-02	4.660125e-03	4.384510e+00	5.605969e+00	3.246485e-01	3.018259e+00	3.336722e+00
9.506716e-05	-1.000000e-01	4.481874e-02	5.649086e-03	4.963041e+00	2.627957e+00	1.752266e+00	2.747075e+00	4.764340e+00

Table 2: Points $K_+^i \in \Sigma_+$ in the shadowing trajectory, for $i = 2, \cdots, 16$. We also tabulate the time t_+ to first cut, the interior time T_{int}, and the time $t_+ + \frac{2\pi}{\nu_{\mathrm{v}}}$ to second cut.

As shown in Table 2, the shadowing trajectory cuts the section Σ exactly once during each passage through the BNF neighborhood U. Therefore, the shadowing trajectory is efficient, because it does not spend extra time orbiting around the equilibrium point L_1.

Remark 9.2. Theorems 3.1 and 3.2 in [8] provide the theoretical foundation for the existence of shadowing orbits similar to the one found numerically in this section. However, as is often the case, the numerical shadowing orbit is beyond the range of applicability of the analytical results. For instance, the homecoming condition (6.4) in Theorem 3.1 is not satisfied, since in our case $N = 17$, $\chi \approx 2.79$, $\lambda \approx \lambda^0 = 2.53$, $\nu_{\mathrm{p}} \approx \nu_{\mathrm{p}}^0 = 2.08$, so

$$(N-1)\chi \approx 44.64 \not< \pi\lambda/\nu_{\mathrm{p}} \approx 3.82.$$

In addition, Theorem 3.2 requires transition maps that correspond to a large number of iterates for the inner dynamics, which is not the case.

10. Two-level differential correction of pseudo-orbits.

In this section, we describe a two-level differential correction method to reduce the discontinuities present in a pseudo-trajectory and apply it to the pseudo-trajectory of Section 9. After convergence of the differential correction method, the converged trajectory is compared with the shadowing trajectory of Section 9.

10.1. Methodology.

A brief overview of the method is given first. More detailed descriptions of this approach may be found in Wilson [26], Pernicka [22], or Parker and Anderson [20]. Using this approach, a level-1 step is taken where velocities at patch points along the trajectory are updated followed by a level-2 step where positions and times are updated.

Level 1. In this step, the variational equations, or the state transition matrix (STM), are computed between a series of *patch points* that have been obtained from another method or model and placed in the current model. The STM is used to update velocities at each patch point so as to target the position at the next patch point.

Level 2. In the level-2 step, positions and times are updated using a least squares approach. Following the derivation in Anderson and Parker, this is computed using

$$\begin{bmatrix} \delta r_1 \\ \delta t_1 \\ \delta r_2 \\ \delta t_2 \\ \delta r_3 \\ \delta t_3 \\ \vdots \\ \delta r_n \\ \delta t_n \end{bmatrix} = M^T (M M^T)^{-1} \begin{bmatrix} \delta \Delta v_2 \\ \delta \Delta v_3 \\ \vdots \\ \delta \Delta v_{n-1} \end{bmatrix}.$$

Here, δr_n is the discontinuity in position at patch point n, δt_n the discontinuity in time, and $\delta \Delta v_n$ the discontinuity in velocity. M is computed from

$$M = \begin{bmatrix} \frac{\partial \Delta v_2}{\partial r_1} & \frac{\partial \Delta v_2}{\partial t_1} & \frac{\partial \Delta v_2}{\partial r_2} & \frac{\partial \Delta v_2}{\partial t_2} & \frac{\partial \Delta v_2}{\partial r_3} & \frac{\partial \Delta v_2}{\partial t_3} & 0 & 0 & \cdots & 0 & 0 \\ 0 & 0 & \frac{\partial \Delta v_3}{\partial r_2} & \frac{\partial \Delta v_3}{\partial t_2} & \frac{\partial \Delta v_3}{\partial r_3} & \frac{\partial \Delta v_3}{\partial t_3} & \frac{\partial \Delta v_3}{\partial r_4} & \frac{\partial \Delta v_3}{\partial t_4} & \cdots & 0 & 0 \\ \vdots & \vdots & \vdots & \ddots & \vdots & \ddots & \vdots & \vdots & \vdots & \vdots & \vdots \\ 0 & 0 & 0 & 0 & \cdots & \frac{\partial \Delta v_{n-1}}{\partial r_{n-2}} & \frac{\partial \Delta v_{n-1}}{\partial t_{n-2}} & \frac{\partial \Delta v_{n-1}}{\partial r_{n-1}} & \frac{\partial \Delta v_{n-1}}{\partial t_{n-1}} & \frac{\partial \Delta v_{n-1}}{\partial r_n} & \frac{\partial \Delta v_{n-1}}{\partial t_n} \end{bmatrix}$$

This adjusts the positions and times, which introduces discontinuities in the velocities at each patch point.

Overall iteration. The entire process is repeated converging first with the level-1 step until a desired tolerance is met and then with the level-2 step. This is typically continued until the changes in the positions become very small within some tolerance, or until the discontinuities satisfy a convergence criterion. The number of patch points is often selected heuristically and modified depending on how well the process is converging. Constraints may also be added for each patch point as needed for the problem or to aid in convergence.

10.2. Application to SR3BP pseudo-orbit. The two-level differential corrector was applied to the pseudo-orbit of Section 9.3 to obtain a nearly continuous trajectory and remove position and velocity discontinuities down to a small tolerance. The only constraint was that the initial and final positions were kept constant. The initial case was run with a larger number of patch points, and the number of patch points was reduced as needed.

The pseudo-orbit of Section 9.3 was used as the initial trajectory (see Figure 12b). This trajectory consists of homoclinic segments that start and end at a large distance $\delta = 0.1$ from the center manifold (see Section 9.2). This reduces the duration of the homoclinic segments, but introduces larger ΔVs or discontinuities. For this case, 16 heteroclinics were used with 64 total sub-segments, and the time spent near L_1 is reduced compared to case $\delta = 0.001$. The pseudo-trajectory has total position and velocity discontinuities of 184 005 km and 338 000 km/h, as described in Section 9.3.

The position discontinuities can be seen more clearly in the closer view in Figure 14. Given the large numbers of segments and discontinuities, this is typically a very challenging case for differential correction.

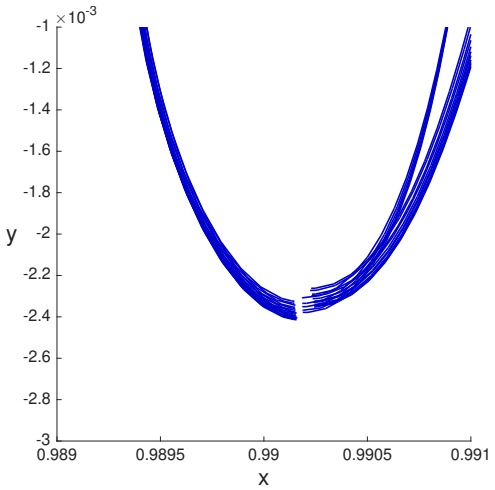
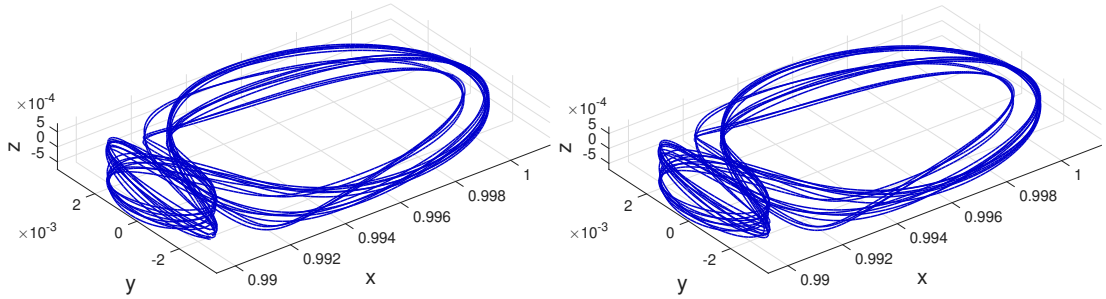


Figure 14: Close xy view of the pseudo-orbit

As a first step in the differential correction process, the segments themselves were used with patch points at each discontinuity. This failed to converge using the typical setup, so intermediate patch points were introduced and then gradually removed as the corrector converged. This process has been found to work well in other cases with long trajectories, and is often used in combination with a reduced correction step size to improve convergence. For this particular case, 400 initial patch points were used with an approximate position update factor of 0.001. Patch points were then interactively added or removed in subsequent steps until a converged solution was found with 40 patch points. The final converged trajectory from the two-level corrector is compared to the original pseudo-orbit in Figure 15. The converged trajectory had total position and velocity discontinuities of 29 m and 0.006 m/s, respectively. This final trajectory was compared to the shadowing trajectory obtained with the multiple-shooting method of Section 9.3 in Figures 16 and 17. Although there is some difference in the phasing of the trajectory, it can be seen that both methods converged to a similar final trajectory. The largest differences are seen in small variations in the z component, and near the beginning of the trajectory. This difference at the beginning might be expected because the differential corrector solution held the positions constant at the initial and final patch points.

These results demonstrate that the pseudo-orbit process described in this paper can generate accurate initial guesses for higher fidelity studies.



(a) Pseudo-Orbit (b) Converged Trajectory

Figure 15: The short trajectory converged using the two-level differential corrector compared to the original pseudo-orbit.

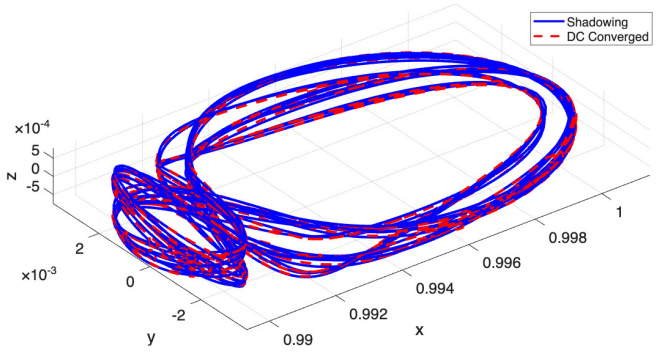


Figure 16: Comparison of the trajectory obtained using the two-level differential corrector and the shadowing method.

REFERENCES

[1] R. L. Anderson, S. Campagnola, and B. B. Buffington, *Analysis of petal rotation trajectory characteristics*, Journal of Guidance, Control, and Dynamics, 41 (2018), pp. 827–840.

[2] V. Arnold, *Instability of dynamical systems with several degrees of freedom*, Sov. Math. Doklady, 5 (1964), pp. 581–585. See also *Vladimir I. Arnold—collected works. Vol. I*, Springer-Verlag, Berlin, 2009, pp. 423–427, DOI 10.1007/978-3-642-01742-1, or *Hamiltonian Dynamical Systems*, edited by R.S MacKay, J.D Meiss, CRC Press, 2020, pp. 633–637, DOI 10.1201/9781003069515.

[3] R. Bowen, *Equilibrium states and the ergodic theory of Anosov diffeomorphisms*, vol. Vol. 470 of Lecture Notes in Mathematics, Springer-Verlag, Berlin-New York, 1975.

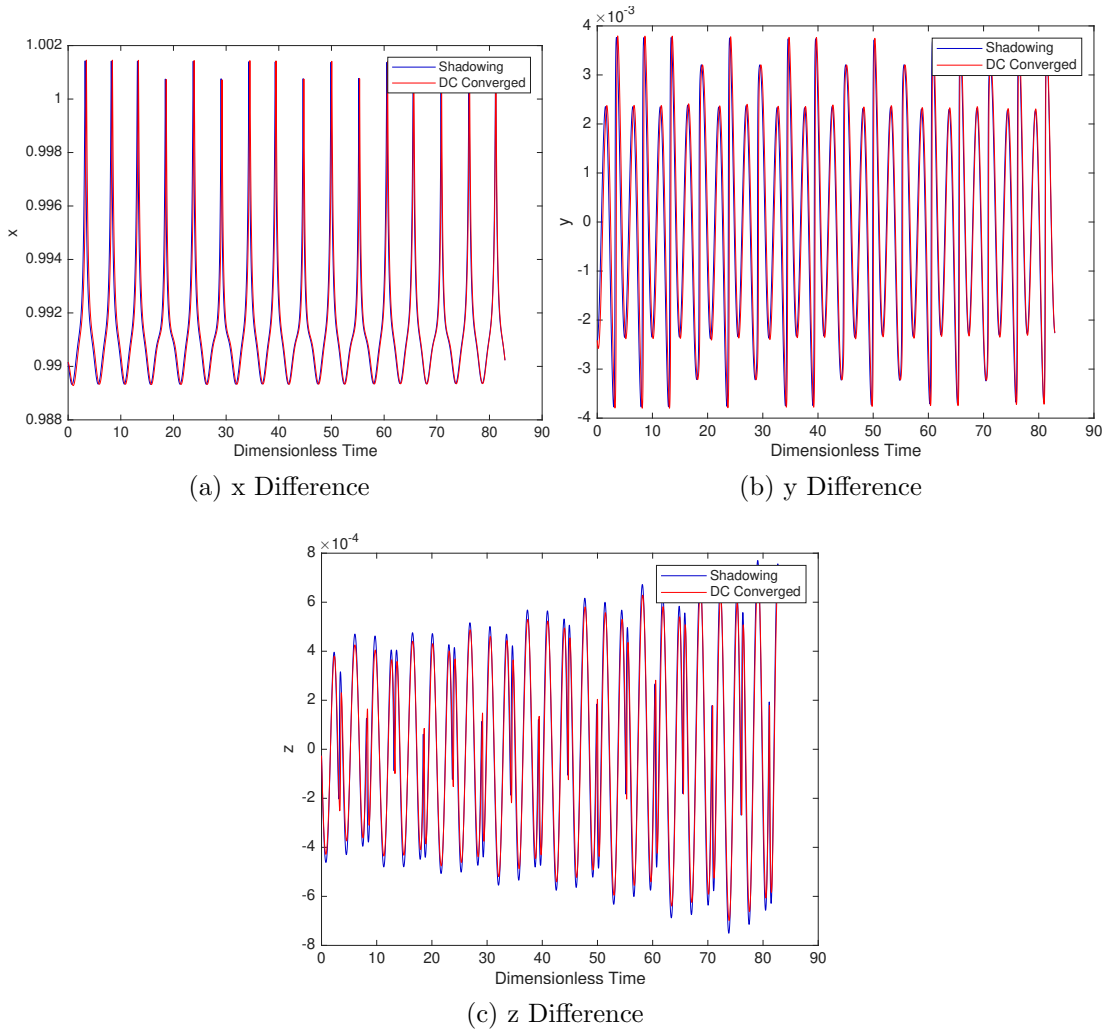
[4] E. Canalias and J. J. Masdemont, *Homoclinic and heteroclinic transfer trajectories between planar Lyapunov orbits in the Sun-Earth and Earth-Moon systems*, Discrete Contin. Dyn. Syst., 14 (2006), pp. 261–279, https://doi.org/10.3934/dcds.2006.14.261, https://doi-org.recursos.biblioteca.upc.edu/10.3934/dcds.2006.14.261.

[5] A. Delshams, R. de la Llave, and T. M. Seara, *A geometric approach to the existence of orbits with unbounded energy in generic periodic perturbations by a potential of generic geodesic flows of* $\mathbf{T}^2$, Comm. Math. Phys., 209 (2000), pp. 353–392, https://doi.org/10.1007/PL00020961, https://doi.org/10.1007/PL00020961.

[6] A. Delshams, M. Gidea, and P. Roldán, *Transition map and shadowing lemma for normally hyperbolic invariant manifolds*, Discrete Contin. Dyn. Syst., 33 (2013), pp. 1089–1112, https://doi.org/10.3934/dcds.2013.33.1089, https://doi-org.recursos.biblioteca.upc.edu/10.3934/dcds.2013.33.1089.

[7] A. Delshams, M. Gidea, and P. Roldan, *Arnold's mechanism of diffusion in the spatial circular restricted three-body problem: a semi-analytical argument*, Phys. D, 334 (2016), pp. 29–48, https://doi.org/10.1016/j.physd.2016.06.005, https://doi-org.recursos.biblioteca.upc.edu/10.1016/j.physd.2016.06.005.

[8] A. Delshams, M. Gidea, and P. Roldan, *Effective shadowing of transition maps for a Hamiltonian saddle-center-center equilibrium. Part I: analytical results.* Preprint at https://web.mat.upc.edu/



(a) x Difference

(b) y Difference

(c) z Difference

Figure 17: Difference in position of shadowing and DC-converged trajectory over time.

amadeu.delshams/articles/DRG26SOTM1.pdf, 2026.

[9] A. Delshams, M. Gidea, and P. Roldan, *Semi-analytic construction of global transfers between quasi-periodic orbits in the spatial R3BP*, Commun. Nonlinear Sci. Numer. Simul., 152 (2026), pp. Paper No. 109220, 34, https://doi.org/10.1016/j.cnsns.2025.109220, https://doi-org.recursos.biblioteca.upc.edu/10.1016/j.cnsns.2025.109220.

[10] A. Giorgilli, A. Delshams, E. Fontich, L. Galgani, and C. Simó, *Effective stability for a Hamiltonian system near an elliptic equilibrium point, with an application to the restricted three-body problem*, J. Differential Equations, 77 (1989), pp. 167–198, https://doi.org/10.1016/0022-0396(89)90161-7, https://doi-org.recursos.biblioteca.upc.edu/10.1016/0022-0396(89)90161-7.

[11] G. Gómez, J. Llibre, R. Martínez, and C. Simó, *Dynamics and mission design near libration points. Vol. I.*, vol. 2 of World Scientific Monograph Series in Mathematics, World Scientific Publishing Co., Inc., River Edge, NJ, 2001, https://doi.org/10.1142/9789812810632_bmatter, https://doi-org.recursos.biblioteca.upc.edu/10.1142/9789812810632_bmatter. Fundamentals: the case of collinear libration points, With a foreword by Walter Flury.

[12] G. Gómez, J. Masdemont, and C. Simó, *Quasihalo orbits associated with libration points*, The Journal of the Astronautical Sciences, 46 (1998), pp. 135–176, https://doi.org/10.1007/BF03546241, https://doi.org/10.1007/BF03546241.

[13] H. Koçak, K. Palmer, and B. Coomes, *Shadowing in ordinary differential equations*, Rend. Semin. Mat. Univ. Politec. Torino, 65 (2007), pp. 89–113.

[14] W. S. Koon, M. W. Lo, J. E. Marsden, and S. D. Ross, *Shoot the moon*, in AAS/AIAA Astrodynamics Specialist Conference, no. AAS 00-166, Clearwater, Florida, January 23-26 2000.

[15] W. S. Koon, M. W. Lo, J. E. Marsden, and S. D. Ross, *Dynamical Systems, the Three-Body*

Problem and Space Mission Design, Marsden Books, 2008, https://www.researchgate.net/publication/328913173_Dynamical_Systems_the_Three-Body_Problem_and_Space_Mission_Design.

[16] M. W. Lo, *Making space travel simpler with the interplanetary highway*, Spaceflight Now, (2002).

[17] M. W. Lo, B. G. Williams, W. E. Bollman, D. Han, Y. Hahn, J. L. Bell, E. A. Hirst, R. A. Corwin, P. E. Hong, K. C. Howell, B. Barden, and R. Wilson, *Genesis mission design*, The Journal of the Astronautical Sciences, 49 (2001), pp. 169–184.

[18] M. W. Lo, B. G. Williams, W. E. Bollman, D. Han, Y. Muellerschoen, D. Cruikshank, and B. Roby, *Genesis mission design*, The Journal of the Astronautical Sciences, 49 (2001), pp. 169–184.

[19] B. H. May, *A Survey of Radial Velocities in the Zodiacal Dust Cloud*, PhD thesis, Imperial College, London, 2007.

[20] J. S. Parker and R. L. Anderson, *Low-Energy Lunar Trajectory Design*, vol. 12 of JPL Deep Space Communications and Navigation Series, John Wiley & Sons, Inc., Hoboken, New Jersey, 1st ed., June 2014.

[21] J. S. Parker, T. P. McElrath, R. L. Anderson, and T. H. Sweetser, *Trajectory design for moonrise: A proposed lunar south pole-aitken basin sample return mission*, Journal of the Astronautical Sciences, 62 (2015), pp. 44–72.

[22] H. J. Pernicka, *The numerical determination of lissajous orbits in the circular restricted three-body problem*, master's thesis, Purdue University, December 1986.

[23] W. T. Reach, B. A. Franz, and J. L. Weiland, *The three-dimensional structure of the zodiacal dust bands*, Icarus, 127 (1997), pp. 461–484.

[24] J. Stuart, R. L. Anderson, C. Sullivan, and N. Bosanac, *Accessing highly out-of-ecliptic science orbits via low-energy, low-thrust transport mechanisms*, in AAS/AIAA Astrodynamics Specialist Conference, no. AAS 19-728, Portland, ME, August 11–15 2019.

[25] K. Wenzel, *The ulysses mission - a voyage to the poles of the sun*, Nuclear Physics B - Proceedings SUpplements, 39 (1995), pp. 59–68.

[26] R. S. Wilson, *Derivation of differential correctors used in genesis mission design*, IOM 312.I-03-002, Jet Propulsion Laboratory, 2003.